A MULTIPLE HEIGHT-TRANSFER INTERFEROMETRIC TECHNIQUE AND ITS APPLICATIONS

by

Hao Yu

A dissertation submitted in partial fulfillment
of the requirements for the degree of
Doctor Of Philosophy
(Mechanical Engineering)
in The University of Michigan
2012

Doctoral Committee:

Professor Jun Ni, Chair
Professor Albert J. Shih
Professor Keith Riles
Assistant Professor Tal E. Carmon
Carl C. Aleksoff, Coherix Inc.

To my beloved family, especially my wife Sibo Hu and my daughter Angela Yu.

ACKNOWLEDGMENTS

I would like to express my sincere gratitude to my PhD advisor Professor Jun Ni for his guidance, advice and encouragement through my research and dissertation. Thanks to him, I have the opportunity to do my PhD in the S. M. Wu Manufacturing Research Center and work on NIST ATP project that gave me great industry experiences. Without his continuous support, this dissertation would have not been accomplished.

I am deeply grateful to Dr. Carl Aleksoff, consulting senior photonics scientist of Coherix, Inc., who is my industry supervisor. He has contributed to the dissertation significantly. He has always had time to discuss the details of my projects, researches and papers, and give invaluable pieces of advice. My gratitude also goes to Mr. Dwight Carlson, Dr. Bin Li, Dr. Zhenhua Huang and many other gentlemen in Coherix, Inc. for their generous and unreserved support.

The kind help from all the other committee members Professor Albert Shih, Professor Keith Riles, and Professor Tal Carmon, are greatly appreciated.

Much appreciation to my dear friends, Yi Liao, Xiaoning Jin, Jie Zhu, Shiming Duan, Jae Wook Oh, Chaoye Pan, Lijung Tai, Kuenren Chen, Adam John Brzezinski, Seungchul Lee, Xin Weng, Xinran Liang, Xun Liu, Guang Dong, Jin Yan. Most of the friends have put up with me for the last 4 years with me in the same office. Also, there

are all the other friends I've made, the list is too long to mention but their friendships are thankful.

My family always stood behind me through the four year PhD study, no matter up or down. Without their support, I could not make this dissertation happen.

TABLE OF CONTENTS

LIST OF FIGURES

LIST OF TABLES

LIST OF ABBREVIATIONS/SYMBOLS

λ	optical wavelength
v	optical frequency
f	measured frequency
γ	frequency tuning rate
G	physical length (thickness)
$U(x)$	uncertainty of a variable x
Λ	Synthetic Wavelength
ADI	Absolute Distance Interferometry
AFR	Ambiguity Free Range
BS	Beam Splitter
ECDL	External Cavity Diode Lasers
FT	Fourier Transform
LSM	Least Square Method
LSF	Least Square Fitting
MHTIT	Multiple Height Transfer Interferometric Technique
MWI	Multiple-Wavelength Interferometry
OPD	Optical Path Difference
OPL	Optical Path Length
PHRF	Power Height Response Function
PM	Polarization Maintaining
ppm	Part Per Million
PSI	Phase Shifting Interferometry
PZT	Piezoelectric Transducer
SNR	Signal-To-Noise Ratio
WSI	Wavelength Scanning Interferometry

ABSTRACT

Absolute distance interferometric metrology is one of the most useful techniques for dimensional measurements. Without movement, measurements can be made without ambiguity, by using either one or several synthetic wavelengths. Synthetic wavelengths result from the beating of two or more wavelengths in multiple-wavelength interferometry (MWI), or a wavelength scan in wavelength-scanning interferometry (WSI). However, conventional MWI requires accurate wavelength information for a large measurement range, while WSI is limited by a mode-hop-free laser tuning range.

A multiple height-transfer interferometric technique (MHTIT) is proposed based on concepts from both MWI and WSI. Using multiple accurately calibrated reference heights, this technique preserves the capabilities to determine the optical path difference (OPD) unambiguously without accurate wavelength information, and yet does not require the laser to be continuously tuned. A multiple reference height calibration artifact is proposed and installed in a holographic measuring system. The design applies OPDs between five closely spaced retroreflectors mounted on a superinvar base plate, which eases alignment and makes it insensitive to temperature changes. Applying the MHTIT with the calibration artifact, the metrology system measurement range is increased from 5 mm to over 100 mm without accurate wavelength information. Three-dimensional images of discontinuous surface heights

obtained from a variety of automotive parts demonstrate the applicability of the MHTIT in workshop environments.

We present an uncertainty analysis, analyzing the primary sources of uncertainties that limit the performance of the MHTIT and discuss how errors can be minimized. The measurement uncertainty is experimentally demonstrated to be about 0.3 μm for 50.8 mm at a confidence level of 95% for two discontinuous surfaces under lab environments.

Another application of the MHTIT for measuring the thickness of a transparent plate is investigated. WSI can measure the thickness of transparent plates by differentiating OPDs from multiple surface interferences in the Fourier domain. However, nonlinear laser tuning deviates the measurement result from the correct value. We propose a wavelength-stepping method for application to thickness measurements of transparent plates. Systematic errors caused by nonlinearity in laser source stepping are reduced with accurate synthetic wavelengths measured by the MHTIT. A 10-μm step height standard etched on a 25 mm × 25 mm × 3 mm quartz block is measured to demonstrate the proposed method with sub-micron accuracy.

CHAPTER 1
INTRODUCTION

1.1 Background and Motivation

Effective measurement methods are critical in precision manufacturing, such as for the auto industry, in order to improve product quality and reducing warranty costs. For automobile bodies and sub-assemblies, optical measurement technologies have revolutionized dimensional quality monitoring and control over the past two decades. The optical measurement systems enable in-line, 100% inspection and the use of advanced statistical analysis methods for root cause diagnostics. Such success has not yet been realized in the automotive powertrain manufacturing. The automotive powertrain includes the engine, engine accessories, transmission, differentials and axles. Usually they have more stringent dimensional and geometrical form tolerances compared with body parts in order to meet their performance requirements, which adds difficulty for metrology instruments.

The conventional Coordinate Measuring Machine (CMM) is a flexible and accurate measurement system that has been extensively used for the inspection of automotive powertrain components. CMM is not feasible, however, for in-line inspection due to the extended measurement cycle time and the lack of a full surface measurement capability, meaning that some critical regions may be neglected. Furthermore, quality control and root

cause diagnostics is also difficult from the incomplete data measured by CMM. In powertrain manufacturing, there are no in-line and full surface measurement and inspection alternatives. However, recent advancements in laser interferometric measurement techniques have shown potential.

Compared to other optical measurement methods, such as time of flight (Kilpelä, et al., 2001), laser triangulation (Fraser, 1992), Moiré (Kafri & Glatt 1989; Wykes & Morshedizadeh 1995), stereovision (Zollne, et al., 2003) and structured lighting (Zou, et al., 1995; Wan & Nosekabel 1999), interferometry (Trolinger 1996; Hariharan 2003), absolute distance interferometry has several simultaneous advantages that make it well suited for the precision manufacturing industry. The advantages include: (1) High accuracy. Combined with phase shifting analysis, interferometric methods can easily achieve micron level or better accuracy. (2) Interferometric measurements can be operated on rough surfaces (Fercher, et al., 1985; Groot 1991) since each pixel can be handled independently and no spatial relationship between pixels is needed to extract phase information. (3) Neither shadowing nor occlusion that is the problem of the stereovision method exists in the laser interferometry, because the object can be illuminated and viewed from the same direction. (4) There are no moving parts in the absolute distance interferometry. The 3D image of the entire field of view is generated without scanning. With all parts being fixed, the system has high reliability and repeatability.

The Coherix ShaPix Surface Detective^{TM} System (Aleksoff, 2006) is a three-dimensional measuring system applying absolute distance interferometric metrology. It shows the potential capabilities for in-line, full surface measurement of powertrain

components. This system can measure surface flatness, parallelism and distances between surfaces with the accuracy of one micron in height measurements (Coherix, 2011). The CCD camera has a 2048×2048 pixel sensor leading to a resolution of 150 µm per pixel in XY for a maximum field of view of 300 mm × 300 mm. And the measurement cycle time is within 1 minute. Fig. 1.1 shows a V10 engine block combustion deck flatness measurement by ShaPix Surface Detective™. Because the part is larger than the field of view, three views on the deck surface are captured and registered together.

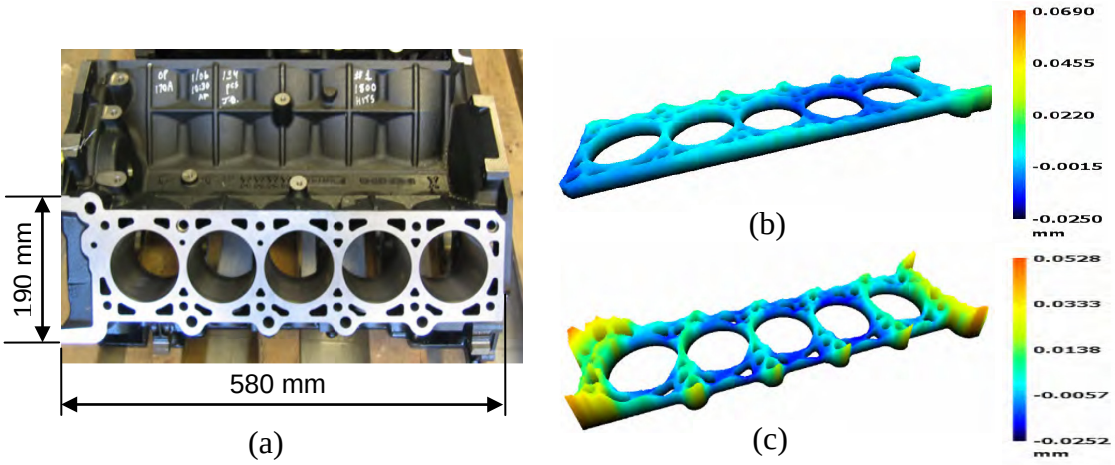

Fig. 1.1 V10 engine block flatness measurement: (a) Overview, (b) New mill and (c) After 1800 milling cycles

Another example shown in Fig. 1.2 presents the dimensional measurement capability for a bipolar plate used in fuel cells. The flatness and parallelism between the surfaces are critical for assembling the fuel cell components to avoid leakage and distortion of the surfaces. As shown in Fig. 1.2 (c) and (d), the flatness of individual surface and height difference between any two surfaces can be easily extracted and analyzed with 1 µm accuracy (Coherix, 2011).

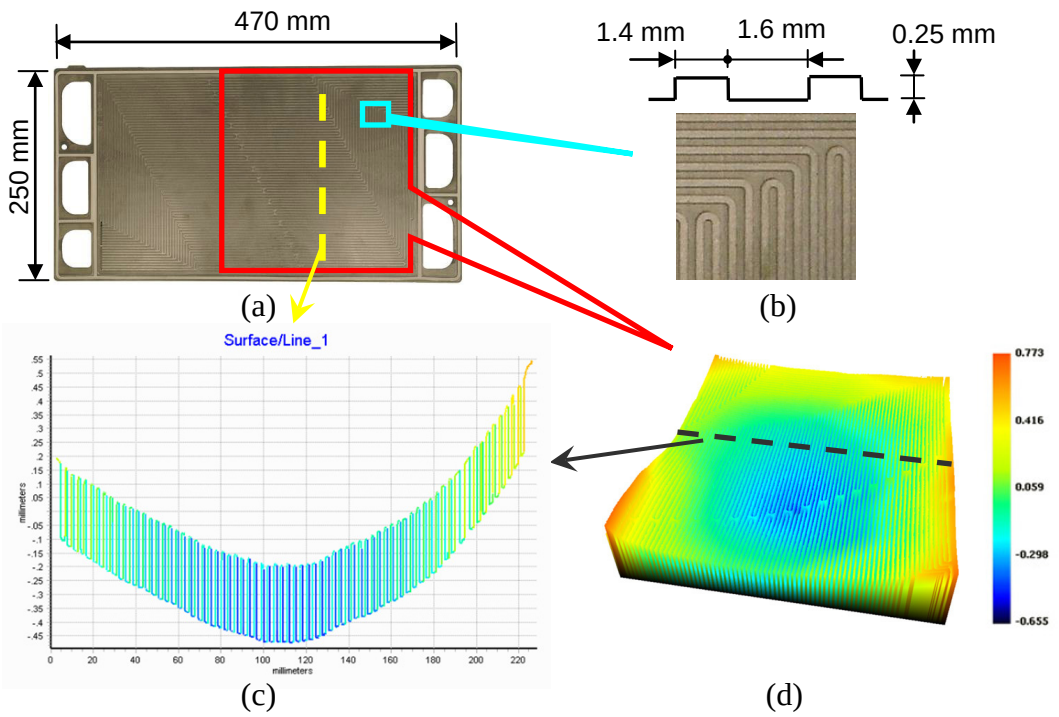

Fig. 1.2 Bipolar plate form and dimensional measurement: (a) Bi-polar plate overview, (b) Close up view of the channels, (c) Cross-sectional measurement and (d) Overall plate dimension

However, the ShaPix system faces significant challenges in achieving larger measurement range with sub-micron measurement accuracy. Industrial applications require large measurement ranges for important features, such as the distance between two critical surfaces of a valve body or a torque convertor housing etc. The current measurement range is limited because the commanded tunable laser wavelengths are not accurate enough to directly measure larger depth ranges. Typically, larger ranges require finer frequency knowledge. One solution is to use an external wavelength meter to accurately measure the frequency of the laser. A commercial wavelength meter can be incorporated as a part of the tunable laser to give the required readout accuracy (<1 pm), but increases the cost of the system. Therefore, an alternative technique that can solve the problem with a low cost is required to improve applicability of the ShaPix

system in precision manufacturing so that it can be broadly adopted for in-line, 100% inspection.

1.2 Research Objective and Framework

The objective of this research is to develop an interferometric measurement technique that increases the measurement capabilities for absolute distance metrology. By applying the proposed technique, the measurement range and accuracy of an interferometric measurement system are significantly improved. Consequently, the system can be widely accepted in precision manufacturing for in-line, full surface inspection due to the extended measurement range and the improved accuracy. In addition, we want to study the measurement uncertainties, analyze the primary sources of the uncertainties, and discuss how errors can be minimized. Furthermore, the application of the proposed method to another related field also will be investigated. Therefore, to increase absolute distance interferometric measurement capabilities, the following problems have been considered in this research:

Absolute distance measurements can be implemented by multiple-wavelength interferometry (MWI) or wavelength-scanning interferometry (WSI). For MWI, a large measurement range requires accurate wavelength information. For WSI, a wavelength scan is used to measure a large distance without accurate wavelength information by comparing the phase shift of an unknown length with respect to a reference length. However it requires expensive cameras for the fast scan and is limited by the mod-hop-free range. Both techniques have some limitations achieving a large measurement range for industrial applications due to the cost issue. But it would be promising to find a way

to combine the complementary advantages for both techniques. In other words, the proposed method can relax the requirement of knowing the accurate wavelength information for MWI using reference interferometers while still taking measurements at multiple discrete wavelengths.

One of the main challenges in the proposed idea is the phase ambiguity induced by the large wavelength difference, i.e., when wrapped phases of the reference interferometer are extracted at different wavelengths, the phase shifts between wavelengths can be larger than 2π leading to an ambiguity problem. In this study, we propose a unique phase unwrapping algorithm using multiple reference heights, which are calibrated to serve as measurement references. This phase unwrapping algorithm, related phase retrieval method, and multiple-wavelength measurement algorithm will be discussed in detail. On the other hand, the design of this reference array needs to be considered in several aspects for long term reliable operations, which include the selection of the number and spacing of the reference array, insensitivity to environmental disturbances, ease of phase extraction and robustness to alignment errors.

This dissertation is organized as follows.

In Chapter 2, a literature review of absolute distance interferometry (ADI) is presented. Two main implementations, MWI and WSI, are explored when used with a tunable laser. Both pros and cons of these two types of techniques are discussed. The underlying aim is to show the absence of a technique that measures a large distance without requiring accurate wavelength information nor a wavelength sweep.

In Chapter 3, the principle of a proposed multiple height-transfer interferometric technique (MHTIT) is explained, which combines the advantages of both MWI and

WSI for industrial applications. The construction of a multiple reference height calibration artifact using retroreflectors mounted on a superinvar base is presented. Applying the MHTIT with the reference array, successful measurements of 101.6 mm gauge block with sub-micron accuracy demonstrate the feasibility of the technique. Three-dimensional images of measurement results of two powertrain parts show the applicability of the technique in industrial applications.

In Chapter 4, repeated gauge block measurement results under the lab environment are presented applying the MHTIT, showing about 0.3 μm uncertainty for a 50.8 mm height step measurement at a confidence level of 95%. We present an uncertainty analysis, discuss sources of errors that are characteristic of MHTIT measurements and propose ways to minimize the errors.

In Chapter 5, another application of the MHTIT to wavelength-stepping interferometry is investigated. The thickness measurement of a transparent plate is achieved using a discrete Fourier analysis in the measuring system. The MHTIT is applied to reduce systematic errors caused by nonlinearity in laser source stepping. The experimental result of measuring a 10-μm step height standard precisely etched on a 50 mm × 50 mm × 3 mm quartz block is presented to verify the proposed method.

Finally Chapter 6 summarizes the contributions of the work. In addition, possible topics for future research work are discussed.

CHAPTER 2
REVIEW OF ABSOLUTE DISTANCE INTERFEROMETRY

2.1 Theory of Interferometric Measurement

Interferometry (Born & Wolf 1999; Goodwin & Wyant 2006) is a powerful tool that provides measurement capabilities ranging from Angstroms to millions of miles. The principle of length measurement by interferometry is straightforward. It is the comparison of a physical length (or a distance in space) against a known wavelength of light. The fundamental relationship of optical interferometry (Gåsvik, 2002) can be expressed in Eq. (2.1).

$$d = N\lambda = (m+e)\lambda \tag{2.1}$$

Where, d is the distance or length being measured, λ is the wavelength, N is the fringe order, m corresponds to the integer part of N and e is its fraction part ($0<e<1$). Commonly the optics are arranged such that the light beam measures exactly double the required length (i.e., it is a double-pass system), in which case one interference fringe period corresponds to a distance or length equal to $\lambda/2$.

Due to the short wavelength of light, the sensitivity of a single wavelength interferometric measurement is very high. The wavelength of light is typically 400-700 nm when visible light is used. By careful analysis of interference fringes, it is possible

to measure e to a resolution of 1/100-1/1000 fringe, resulting in nm or sub-nm measurement.

However, also due to the short wavelength of the light, the distance or length between two measuring points must be smaller than a half-wavelength unless additional information is provided. This limitation arises from the sinusoidal nature of optical interference. In a single wavelength interferometric measurement, the phase of the light, and hence the phase of the interference pattern, repeats itself at distance intervals equal to the wavelength. Thus, a distance d gives the same interferometric measurement as ($m\lambda/2+d$). Since all optical fringes are identical, for classical interferometers (mainly Michelson type), the only way to conduct a measurement for a length or distance larger than $\lambda/2$ is to count fringes while the target moves along the length to be measured. The main disadvantage of using a fringe counting system is that it provides only relative measurements of distance and requires a continuous counting method.

Compared to relative measurement methods, the advantage of absolute distance interferometry (ADI) is the ability to make length measurements without the need for continuous fringe counting or moving parts in the measuring interferometer. This allows for an interferometer design which is simpler, more compact and rugged, as required by many metrology applications. Various techniques for performing absolute distance interferometric (ADI) measurements have been proposed in the literature (Bourdet, 1979; Gillard, 1982; Margheri, 1997; Bechstein, 1998; Barwood, 1998; Kinder, 2002; Ye, 2004). There are two implementations of ADI measurements, which are multiple-wavelength interferometry (MWI) and wavelength-scanning interferometry (WSI). A synthetic wavelength is generated in both cases, either from the beating of two

wavelengths or a wavelength sweep, which is much larger than the optical carrier wavelength.

2.2 Multiple Wavelength Interferometry

Two-wavelength interferometry was first proposed over 3 decade ago to solve the ambiguities of determining the integer number of wavelength in a distance measurement (Polhemus, 1973; Cheng & Wyant, 1984; Creath, 1987). The typical system setup is a Michelson interferometer. The measurement is performed at two wavelengths, and the measurement results are compared for the different wavelengths to determine the true distance. For example, if two close wavelengths λ_1 , λ_2 are used, the OPD is measured by the synthetic wavelength Λ rather than a single wavelength. The synthetic wavelength Λ is expressed in Eq. (2.2).

$$\Lambda = \frac{\lambda_1 \lambda_2}{\lambda_1 - \lambda_2} \tag{2.2}$$

It is larger than either wavelength and thus can measure a longer range without incurring the 2π phase wrap. Theoretically, two close enough wavelengths are sufficient to measure any height (Groot, 1994). However, the resolution of two-wavelength interferometers can be much worse than what can be obtained in a single wavelength interferometer. This is mainly due to the scale difference between synthetic wavelength (tens of millimeters) and the optical wavelength (fractions of a micrometer) leads to noise amplification. Thereby, more wavelengths with large interval between them are introduced to decrease the synthetic wavelength and guarantee a good precision while achieving a large height measurement range.

The accuracy of a distance measurement by MWI depends primarily on the properties of the laser source (coherence, stability, and power) and on the calibration of the synthetic wavelength. Hence, breakthroughs in the MWI techniques were preceded by breakthroughs in the development of multiple-wavelength laser sources. Many gas lasers have been selected as sources due to their advantages of emitting light at different wavelengths. For instance, CO_2 lasers emit at a large number of wavelengths between 9 μm and 11 μm, corresponding to transitions for the various vibrational-rotational energy levels. Bourdet & Orszag (1979) measured a length of 50 cm with an accuracy of 0.1 μm. He-Ne lasers, which are traditionally used in most high-performance interferometers, can also be applied to MWI, using different laser lines, e.g., at 629.4 nm and 632.8 nm (Dändliker, et al. 1995). Other gas lasers, such as Ar lasers (Dändliker, et al. 1988), He-Xe laser (Matsumoto, 1981) and Kr-ion laser (Fercher, et al. 1985) had also been used in MWI experiments. By applying gas lasers and other specific lasers stabilized on different atomic absorption lines, absolute distance can be determined with very high accuracy using the method of exact fractions (Zhu, 1989; Bitou, 2000; Pförtner, 2003). Lewis (1993) reported a relative measurement uncertainty about 10^{-7} using frequency-stabilized He-Ne operating at 632.990876 nm (red), 543.516364 nm (green) and 611.970617 nm (orange). But one drawback in early MWI development was the limited availability of stabilized laser sources which lead to limited applications in industries.

Tunable lasers are of a great interest for MWI measurements since synthetic wavelengths can be chosen with more flexibility. Compared to cumbersome dye lasers, semiconductor laser diodes have the advantages of high energy efficiency and

compactness. In recent years, commercially available external cavity diode lasers (ECDL) (Harvey, 1991; Luecke, 1994) were often employed for MWI because of its compactness and widely tunable range. Many data processing techniques were developed by different researchers for MWI to achieve a robust and accurate measurement with a large range. Lu & Lee (2002) proposed a variable synthetic wavelength interferometry with an ECDL source generating wavelengths λ_1, λ_2,… λ_n. An unknown OPD is obtained from a series of calculations in terms of synthetic wavelengths and measured synthetic fractional fringes to avoid fringe ambiguity. Every synthetic wavelength is the combination of the varied wavelengths λ_2,… λ_n and the initial wavelength λ_1. At each stage, the OPD is corrected to a new value with a smaller uncertainty than that at the preceding stage. This method requires an iterative calculation, which increases the algorithm complexity and reduces the robustness if many wavelengths are needed to achieve the accuracy due to the environmental disturbances.

Another important multiple-wavelength measurement algorithm uses Fourier transform algorithms to determine the distance value (Marron, 2000; Aleksoff, 2006). The use of Fourier transform methods to determine depth is common in the field of synthetic aperture radar (Marron, 1992; Carrara, 1995). The fundamental relationship employed is the Fourier transform relationship between the wavelength (or frequency) space and the height (or distance) space, which can be written in a discrete form as

$$I(h)=\left|\sum_{n=1}^{N} e^{-2\pi i \nu_n 2h/c+i\phi_n}\right|^2 = N+2\sum_{n=1}^{N}\sum_{m>n}^{N}\cos\left[-2\pi(\nu_n-\nu_m)2h/c+\phi_n-\phi_m\right],$$
$$m,n=1,\ldots,N \tag{2.3}$$

where, *I(h)* is the intensity of the height profile *h* within the measurement pixel, ϕ_n are wrapped phase information at the n^{th} frequency value ν_n, over N frequencies. An illustration of a height profile is shown in Fig. 2.1. This profile shows the normalized return amplitude from the object as a function of height *h*, where *h* is in arbitrary dimensional units.

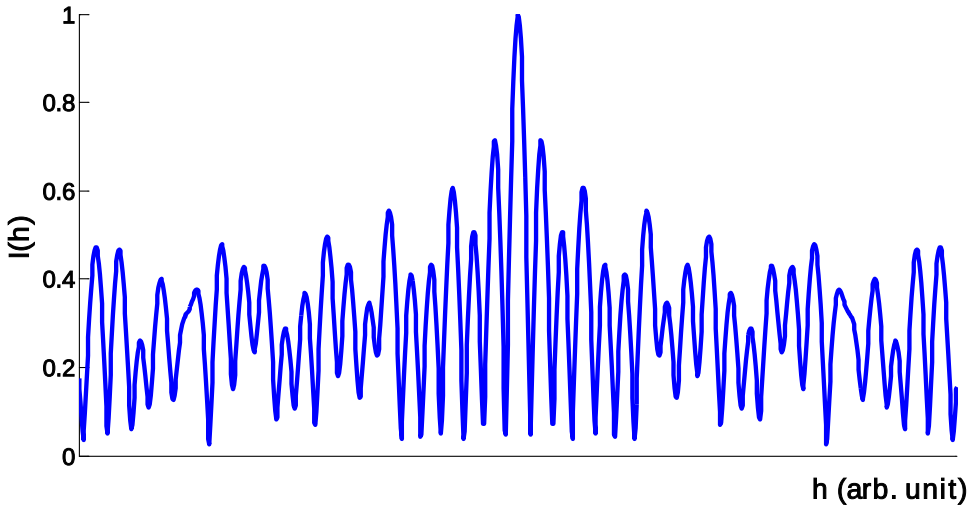

Fig. 2.1 Height intensity profile for a single pixel

With a depth profile as shown in Fig. 2.1, one can determine the relative height of the object *H* by locating the peak return as

$$H=\arg\max(I(h)) \tag{2.4}$$

Using this peak finding algorithm, all the wavelengths can be taken into account simultaneously. However, based on Eq. (2.3), the ambiguity measurement range of this algorithm depends on the stability and the calibration of the different wavelengths. It

means large measurement range can be achieved only by using a wavelength calibration device such as an etalon or a wavemeter, which limits its industrial applications due to system cost and complexity.

Recently, the availability of femtosecond mode-locked lasers has opened new perspectives in the field of accurate and long range absolute distance measurements. Different measurement techniques take advantage of the wide and well-defined frequency grid of femtosecond lasers (Minoshima & Matsumoto, 2000; Jin, et al. 2006; Schuhler, et al. 2006). Ye (2004) proposed to combine a time-of-flight technology with fringe-resolved interferometry to extend the measurement range beyond 10^6 m. Joo and Kim (2006) achieved a 7 nm resolution over 0.89 m using a dispersive channeled spectrum technique. Salvadé, et al. (2008) demonstrated experimentally an accuracy of 8 nm over 800 mm range using frequency comb reference multiwavelength source and a superheterodyne detection technique. However, a mode-locked laser is still expensive, so it is mainly used in the scientific laboratories.

2.3 Wavelength Scanning Interferometry

Wavelength-scanning interferometry (WSI) is another technique enabling absolute distances to be measured unambiguously. This technique is not new, dating back to the 1980s (Olsson 1981, Tansey 1983), but it was not studied extensively until more recently when tunable lasers replaced the cumbersome dye lasers originally employed as a light source (Beheim, 1985; Kikuta, 1986; Boef, 1987; Sasaki, 1991). Of particular interest are the ECDLs with large ranges that have been employed for ADI (Thiel, 1995; Xiaoli, 1998; Stone, 1998; Yang, 2005; Hibino, 2010). It generates the

synthetic wavelengths by scanning the frequency of the laser source within a given sweep range. As the frequency sweeps, detection electronics counts synthetic-wavelength maxima (temporal "synthetic fringes") without ambiguity. Wavelength scanning/shifting interferometry, frequency sweeping/scanning interferometry, swept wavelength interferometry, optical frequency domain reflectometry, frequency modulated continuous wave and variable synthetic wavelength are all synonyms relying on the same basic principles. A typical WSI system set up is also based on a Michelson interferometer shown in Fig. 2.2.

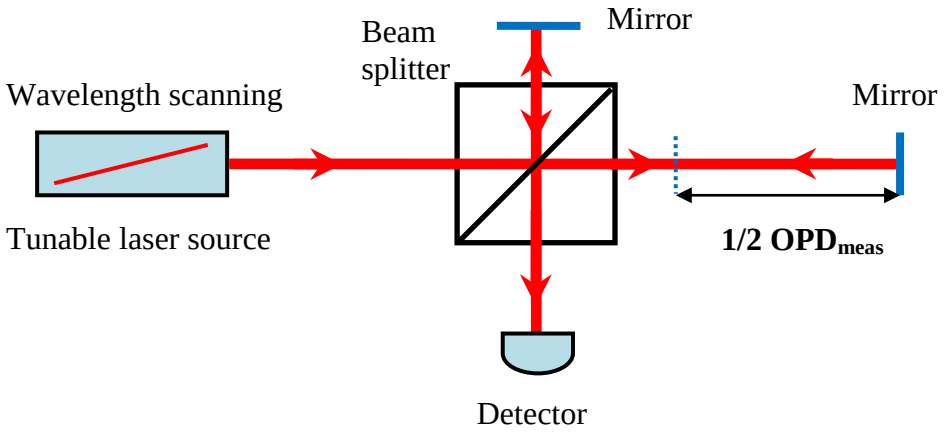

Fig. 2.2 A typical wavelength scanning interferometry setup

In Fig 2.2, a tunable laser source's output light is divided into two beams. Based on the theory of interference, the intensity $I(t)$ of interference pattern on the detector can be expressed by Eq. (2.5).

$$I(t) = a + b\cos[2\pi \frac{OPD_{meas}}{c}(v_0 + \gamma_v t)] \tag{2.5}$$

Where, a represents the background intensity, b represents the modulation intensity, c is the speed of light, v_0 is laser frequency at time t =0 and γ_v is the frequency tuning rate. From the equation, if the laser frequency is perfectly linearly tuned, intensity will vary sinusoidally. A Fourier transform gives the frequency of the intensity variation f_{meas}. Then the measured OPD can be expressed as

$$OPD_{meas} = \frac{cf_{meas}}{\gamma_v} \tag{2.6}$$

This is the fundamental principle behind a distance measurement by WSI. If the optical frequency tuning rate γ_v is not known as *a priori* or has fluctuations, which is the case in most situations, a more commonly adopted system is built with both a reference interferometer and a measurement interferometer as shown in Fig. 2.3.

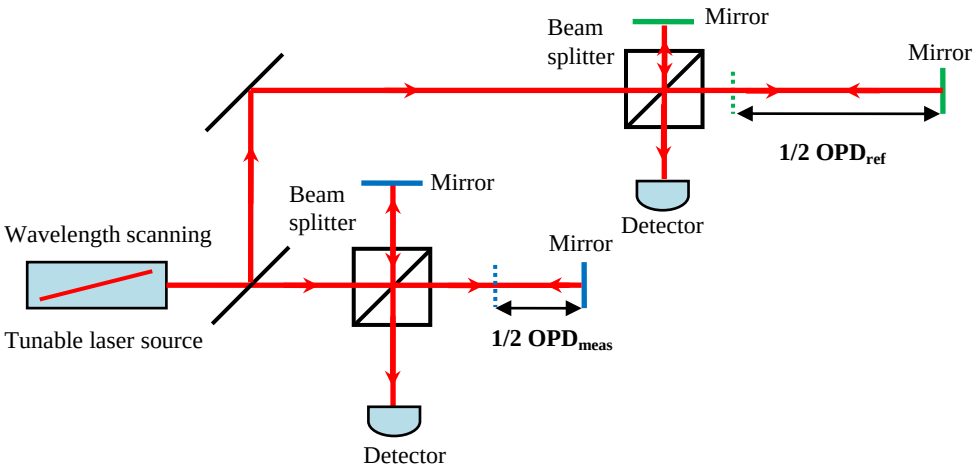

Fig. 2.3 A WSI setup with a reference interferometer

Since two interferometers experience the same wavelength tuning, the interferometer of unknown length OPD_{meas} can be measured by comparing the phase change with the

known reference interferometer OPD_{ref} . By counting the number of the synthetic fringes of both interferometers while the laser wavelength is scanning, OPD_{meas} is determined directly without wavelength information which is shown in Eq. (2.7).

$$\frac{OPD_{meas}}{OPD_{ref}} = \frac{\Delta\phi_{meas}}{\Delta\phi_{ref}} \tag{2.7}$$

Where the phase change $\Delta\phi_{meas}$ and $\Delta\phi_{ref}$ are determined by the number of interference patterns corresponding to the measurement interferometer and the reference interferometer, respectively.

Main error sources of WSI (Kikuta and Nagata, 1987) include non-linear laser tuning, sensitivity to vibrations and environmental disturbances during the experiment. Various approaches have been proposed to reduce the non-linear effects during the tuning such as the use of a reference interferometer (Kobayashi, Takada, & Noda, 1990). The heterodyne technique is effective for reducing the sensitivity to environmental disturbance (Tiziani, 1996; Lu, 2002). More recently, WSI is combined with MWI by using another stabilized laser (Vakhtin, 2003; Krishnamachari, 2006) or another tunable laser (Hartmann, 2008; Pollinger, 2009). An additional reference laser, generally having a common path to the measurement interferometer, is used to generate an interferometric error signal to actively stabilize the measurement optical path with feedback control. Also, a fixed synthetic wavelength can be provided by stabilizing the laser wavelengths to atomic absorption lines. The measurement uncertainty of WSI is then reduced to a fraction of the synthetic wavelength.

To implement WSI with high accuracy, a laser is needed to offer continuous tuning over a wide wavelength range that results in a short synthetic wavelength. However, appearances of mod hops shorten the tuning range and decrease the measurement accuracy. Besides, the scanning process limits its industrial applications in fine resolution, high sample density measurements due to limited frame rate of low cost CCD cameras.

2.4 Summary

Absolute distance measurements can be implemented by MWI and WSI without the need for moving parts in the measuring interferometer. The development of tunable lasers, particularly the emergence of external-cavity diode lasers, provides an opportunity for new implementations of both methods, which are attracted due to their compactness and flexibility of generating synthetic wavelengths. High accuracy measurements with large ranges have been demonstrated by many researchers using MWI. However, MWI requires accurate wavelength information for a large range measurement. Another important technique, WSI, performs the measurement by comparing an interferometer of unknown length with a known length reference interferometer without the necessity of accurate wavelength information. But a wavelength sweep is required in the measurement.

In this study, the measuring system applies MWI, which in theory needs accurate wavelength information for a large step height measurement. It is challenging to apply WSI due to CCD speed limitations whenever fine resolution and high sample density measurement is needed. Therefore, one of the main objectives of this study is to

develop a new technique that can achieve a large measurement range and good accuracy with low cost, thus increasing the applicability of the measuring system in industrial applications.

CHAPTER 3
A MULTIPLE HEIGHT-TRANSFER INTERFEROMETRIC TECHNIQUE

In this study, we propose a multiple height-transfer interferometric technique (MHTIT). This technique provides an effective way to combine multiple-wavelength interferometry (MWI) and wavelength-scanning interferometry (WSI). The technique applies the MWI scheme with discrete measurements at several wavelengths instead of a wavelength scanning process, and employs reference interferometers analogous to WSI to avoid the wavelength accuracy requirement. It takes advantages of multiple reference heights for phase unwrapping. Synthetic wavelengths are obtained from the ratio of the reference height and corresponding phase differences instead of absolute wavelengths in conventional MWI. A modified Fourier transform (FT) peak finding algorithm is proposed to calculate the object height.

The next section discusses the principle of this MHTIT technique in detail. A multiple reference height calibration artifact is then designed, installed and calibrated in the measuring system. Step height measurements of a gauge block are conducted to verify the proposed technique presenting sub-micron accuracy for over 100 mm range. 3D measurement results obtained from a variety of objects are also presented to demonstrate the applicability of this technique.

3.1 Principle

To understand the principle of the MHTIT, consider a Michelson interferometer (Fig.3.1).

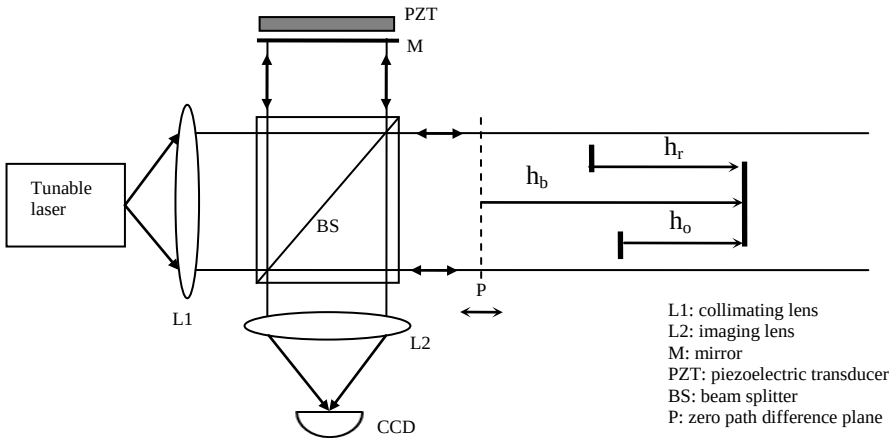

Fig. 3.1 Michelson set-up with reference and measurement interferometers

In a typical Michelson interferometer, laser light is divided between a reference beam and an object beam. The OPD is measured with respect to the zero path difference plane P. However, the location of plane P may drift leading to measurement errors. In such situations, the OPD can be self-referencing by subtracting two optical paths to minimize this effect, which also allows the OPD to be measured far away from the zero path difference plane. As shown in Fig. 3.1, a tunable laser illuminates a reference height h_r section and a height h_o to be measured, both on a common base a distance h_b from the zero path position. The unwrapped phase for the base is given by

$$\Phi_{b,n} = 2\pi q_{b,n} + \phi_{b,n} = \frac{4\pi h_b}{\lambda_n} \tag{3.1}$$

and the reference and object unwrapped phases are given by subtracting corresponding unwrapped phase from Eq. (3.1),

$$\Phi_{s,n} = 2\pi(q_{b,n} - q_{s,n}) + (\phi_{b,n} - \phi_{s,n}) = \frac{4\pi h_s}{\lambda_n} \tag{3.2}$$

where, *s*=*b*, *r* or *o* representing the base, reference or object section, respectively, $q_{b,n}$ and $q_{s,n}$ are unknown integer fringe orders, $\phi_{b,n}$ and $\phi_{s,n}$ are the measured phase information from the zero path position in the range of $(-\pi, \pi]$, and λ_n is the wavelength. The measurement, due to the unknown integer fringe order, is limited to $\Phi_{s,n} < (-\pi, \pi]$ and hence severely limits the measurement range to an ambiguity-free-range (AFR) of $\lambda_n / 2$. However, if a second wavelength λ_m (assuming $\lambda_n > \lambda_m$) is used and we subtract the resulting phases, the result is the synthetic wavelength equation (Cheng & Wyant, 1984)

$$\Delta\Phi_{s,m,n} = 4\pi h_s \left(\frac{1}{\lambda_m} - \frac{1}{\lambda_n}\right) = \frac{4\pi h_s}{\Lambda_{mn}} \tag{3.3}$$

Where, $\Delta\Phi_{s,m,n}$ is the phase difference due to subtracting the unwrapped phases and the synthetic wavelength is given by

$$\Lambda_{m,n} = \frac{\lambda_n \lambda_m}{\lambda_n - \lambda_m} \tag{3.4}$$

The measurement AFR is then extended to $\Lambda_{m,n} / 2$. Theoretically, two close enough wavelengths are sufficient to measure any height. However, noise comes into play and error amplification leads to poor measurement precision. Thereby more wavelengths are introduced to guarantee a good precision while achieving large measurement range. The range of possible laser wavelengths determines the nominal

height measurement resolution. The measurement AFR depends on the stability and the calibration of the different wavelengths. For this reason, the uncertainty of laser wavelengths limits the measurement AFR of MWI. In order to break through this limitation, in this study we apply both reference and measurement heights at multiple wavelengths.

Consider the following relationship attained by dividing one synthetic wavelength equation by the other.

$$\frac{\Delta\Phi_{o,m,n}}{\Delta\Phi_{r,m,n}} = \frac{h_o}{h_r} \tag{3.5}$$

If we assume that $\Lambda_{m,n} / 2 > h_b > h_o, h_r$, then the ratio above does not require phase unwrapping nor depend on the wavelengths directly. Hence, we can solve for h_o, since we know h_r and the measured phases are the same as the unwrapped phase. Also, the variability of the base height is removed. However, noise amplification still limits the practical range. In general, for larger heights a phase unwrapping procedure is required. WSI obtains the phase differences by counting the fringes for both reference and measurement interferometers during the wavelength scan. In this study, we propose two different approaches for phase unwrapping. For the reference phase difference, multiple reference heights are used for phase unwrapping. And for the object phase difference, a modified FT peak finding algorithm is applied to overcome phase wrapping. We now explain these techniques in detail.

3.1.1 Reference Phase Unwrapping

For reference phase unwrapping, considering Eq. (3.3), if we assume phase difference between two wavelengths is less than 2π, that is, $\Delta\Phi < 2\pi$, then the wavelength difference must satisfy the following equation.

$$\left|\lambda_m - \lambda_n\right| < \frac{\lambda_m \lambda_n}{2h} \equiv \Delta\lambda_{m,n} \tag{3.6}$$

The right side of the expression is defined as the wavelength acquisition interval. Here, the height h, is determined by the maximum wavelength difference without introducing phase ambiguity. Small heights have large acquisition intervals and vice versa. Table 3.1 shows the wavelength acquisition intervals and corresponding heights centered at 800 nm wavelength.

Table 3.1 Wavelength Acquisition Interval Centered at 800 nm for Several Heights

Height h (mm)	Wavelength Acquisition Interval $\Delta\lambda$ (pm)
0.5	640
5	64
50	6.4
500	0.64

Consider that the wavelength acquisition interval limits the maximum wavelength difference that can be applied without phase ambiguity. In order to measure h_o with a high accuracy, both small and large reference heights are required. On one hand, a small height needs to be applied for phase unwrapping due to wide wavelength interval/bandwidth, which improves the measurement resolution. On the other hand, the final uncertainty of the measurement has two major contributors: uncertainty of calibration of the reference height and uncertainty of phase difference. A large height is

preferred as the measurement reference in order to decrease the measurement uncertainty. First, it requires less effort to achieve higher relative calibration accuracy compared with a small height in a practical optical system where noises exist. For instance, if the same calibration uncertainty of the reference height 1e-6 is desirable, the required absolute measurement accuracy for 0.5 mm height is 0.5 nm whereas it is 50 nm for 50 mm. Measurement accuracy of 0.5 nm requires about 1/10000 fringe accuracy which is very challenging due to environmental disturbances such as vibration. And it is more practical for an optical system to achieve a 50-nm measurement accuracy for a 50-mm range. Second, with the help of a large height, uncertainty of phase difference will be decreased since the phase change of a larger height is greater than a small one for the same wavelength scan range.

Therefore, a technique applying multiple step heights named MHTIT is proposed. Small reference heights are used to remove phase ambiguity for large reference heights when large wavelength differences are applied. And the longest reference height is employed as the final measurement reference, which provides the best measurement accuracy.

The main challenge of reference phase unwrapping results from uncertainty of laser wavelengths. If two different wavelengths are applied, uncertainty of wavelength difference leads to uncertainty of phase unwrapping for large heights. For example, based on Eq. (3.3) and the center wavelength is 800 nm, a 20 pm uncertainty wavelength difference will cause over 18 radians phase uncertainty for a 50 mm height, whereas only a 0.18 radian phase uncertainty exists for a 0.5 mm height. Hence, we cannot totally rely on the wavelength information to do the phase unwrapping since

wavelength uncertainty for a typical tunable laser is no better than 100 pm. Instead, we choose the proper shortest reference height so that wavelength uncertainty does not cause fringe order ambiguity. Consequently, the fringe order difference can be determined correctly and thus the phase difference for the shortest reference height can be unwrapped. This unwrapped phase information is then used to unwrap the phase difference for next step height and so on using Eq. (3.7) motivated by Eq. (3.5). The process terminates when all phase differences are unwrapped.

$$\frac{h_1}{2\pi q_{n1} + \Delta\phi_{n1}} = \frac{h_2}{2\pi q_{n2} + \Delta\phi_{n2}} = \cdots = \frac{h_{M-1}}{2\pi q_{nM-1} + \Delta\phi_{nM-1}} = \frac{h_M}{2\pi q_{nM} + \Delta\phi_{nM}} \tag{3.7}$$

Here, $h_1, h_2, \ldots h_M$ are multiple heights in ascending heights, q_{n1} is the integer fringe order change from wavelength n to wavelength 1, and $\Delta\phi_{n1}$ is the wrapped phase difference from wavelength n to wavelength 1.

3.1.2 Object Phase Unwrapping

After the phase difference for the longest height h_M is determined, Eq. (3.8) is given at different wavelengths for the object height h_o.

$$\frac{h_o}{2\pi q_n + \Delta\phi_n} = \frac{h_{ref}}{\Delta\Phi_n} \tag{3.8}$$

Where, q_n is unknown integer fringe order change from wavelength n to wavelength 1; h_{ref} is corresponding to the largest height h_M, $\Delta\Phi_n$ is equal to $2\pi q_{nM} + \Delta\phi_{nM}$. In order to calculate object height h_o, a phase unwrapping algorithm is usually needed, which can be very challenging due to the presence of noise. Instead, we propose a modified FT

peak finding algorithm to avoid phase unwrapping and to calculate the object height (Marron 1992, Aleksoff 2006). We reorganize Eq. (3.8) as in Eq. (3.9):

$$2\pi q_n + \Delta\phi_n = \frac{h_o}{h_{ref}}\Delta\Phi_n \tag{3.9}$$

By recognizing that the wrapped phase $\Delta\phi_n$ can be taken into account by using the periodicity of a sinusoid and that the measured phase corresponds to starting phase, we move the wrapped phase $\Delta\phi_n$ to the right hand side of the equation and take the cosine function on both sides as shown in Eq. (3.10)

$$\cos(2\pi q_n) = \cos\left(\frac{h_o}{h_{ref}}\Delta\Phi_n - \Delta\phi_n\right) = 1 \tag{3.10}$$

Since q_n is an integer. Then simply adding the sinusoids together will give a peak signal at the object height regenerated via the following equation.

$$r(h_o) = \sum_{n=2}^{N} e^{i\left(\frac{h_o}{h_{ref}}\Delta\Phi_n - \Delta\phi_n\right)} \tag{3.11}$$

Where, complex exponentials replace sinusoidal functions. The peak of $r(h_o)$ is when h_o equals the actual object height. But the actual position of the peak includes long distance offset, which may not be stable. If one takes the magnitude square of $r(h_o)$, then the highly oscillating carrier term is removed and only the envelope remains. The envelope peak is the derived peak that does not depend on the exact baseline position. This magnitude square is called the power height response function (PHRF):

$$|r(h_o)|^2 = \left| \sum_{n=2}^{N} e^{i\frac{h_o}{h_{ref}}\Delta\Phi_n - i\Delta\phi_n} \right|^2 = N - 1 + 2\sum_{n=2}^{N}\sum_{m>n}^{N} \cos\left[\frac{h_o(\Delta\Phi_n - \Delta\Phi_m)}{h_{ref}} - (\Delta\phi_n - \Delta\phi_m) \right] \quad (3.12)$$

Where, $m, n = 2,..., N$ and the actual object height H is given at the global maximum position shown in Eq. (3.13).

$$H = \arg\max(|r(h_o)|^2) \quad (3.13)$$

An example plot of normalized PHRF over a 10 mm range is shown in Fig. 3. 2.

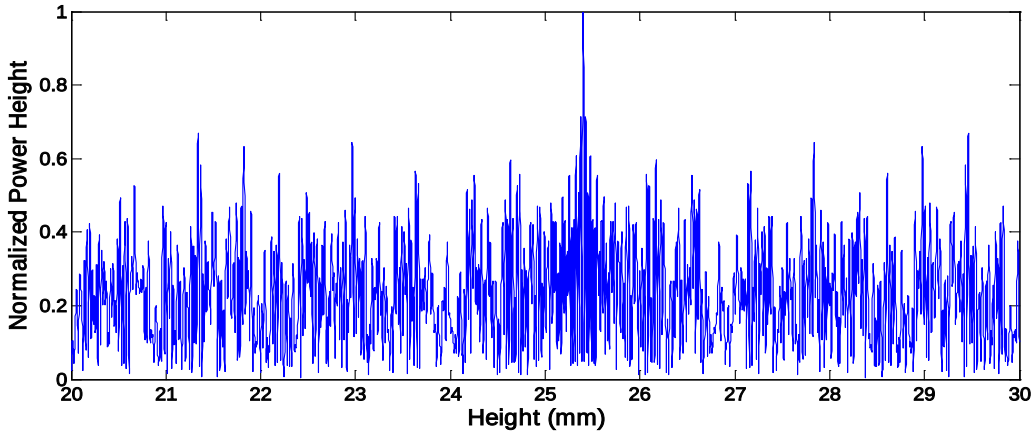

Fig. 3.2 An example plot of power height response function. The location of main peak corresponds to the object height of 25.4 mm and the minor peaks are influenced by the selection of multiple wavelengths and system noise.

Another advantage of using this peak finding algorithm is that the measurement AFR is then determined by the least common multiple of different wavelengths. And the theoretical AFR is only limited by the coherence length of the output laser (Walsh, 1987), which is required to be much longer than the largest synthetic wavelength formed by the two closest wavelengths in MWI.

3.1.3 MHTIT Measurement Procedure

The detailed measurement procedure of MHTIT is shown in Fig. 3.3.

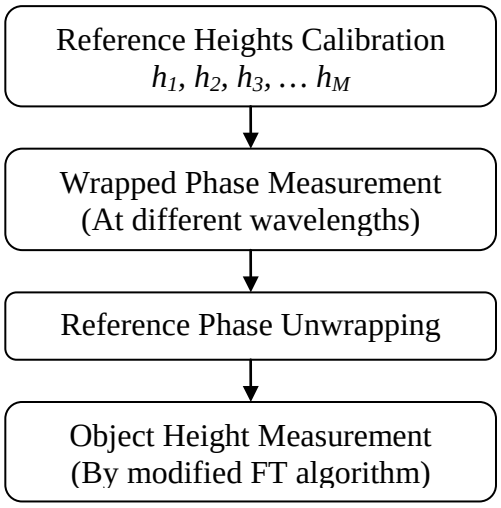

Fig. 3.3 Overview of MHTIT scheme

There are 4 steps for MHTIT measurements. First, the OPDs of reference heights $h_1, h_2, ...h_M$ in the system have to be calibrated accurately. Second, applying different wavelengths, wrapped phases $\phi_1, \phi_2, ...\phi_M$ are measured by phase shifting technique. The third step requires reference phase unwrapping using multiple reference step heights. Finally, a modified FT algorithm is proposed for object height measurement.

In MWI, variable synthetic wavelengths are generated by combinations of the various wavelengths. The object height is thus measured by synthetic wavelength as reference. In MHTIT, the object height is measured using the reference heights and corresponding phase differences as the basis of the measurement. In theory, the ratio of reference heights and total phase differences in MHTIT is equivalent to synthetic wavelengths used in MWI. MHTIT provides an alternative way to find synthetic wavelengths.

3.2 System Description

The metrology system being used for our work is a Coherix ShaPix® system which measures object surface shapes by employing multiple wavelengths generated via a tunable laser (Aleksoff, 2006; 2010). A schematic diagram of the Coherix ShaPix unit is illustrated in Fig. 3.4. It is a holographic interferometric metrology instrument that measures the shape of 300 mm by 300 mm surfaces and larger with stitching. The primary components of interest are: (a) a tunable diode laser; (b) measurement interferometer optics; and (c) a multiple reference height calibration artifact (reference array). These components are described in detail below.

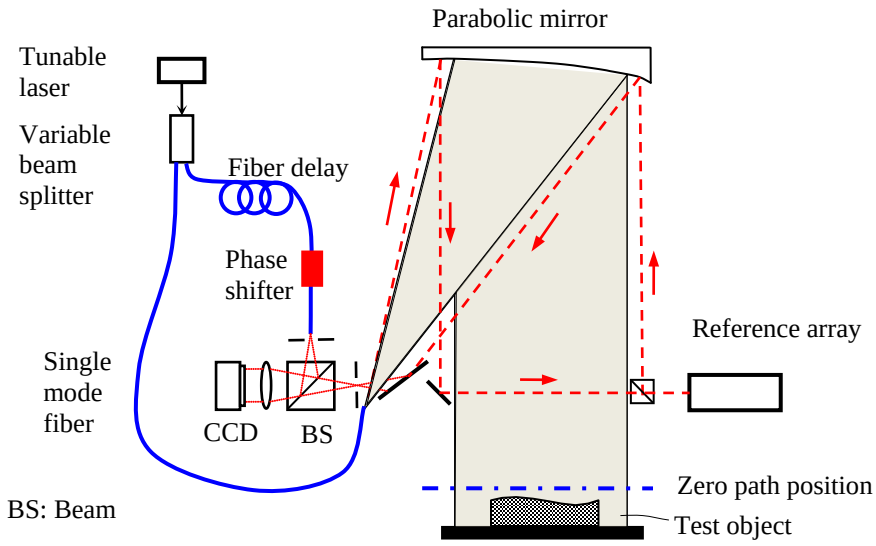

Fig. 3.4 Illustration of the ShaPix holographic metrology system and insertion of the reference array using excess light and pixels

3.2.1 Laser Source

The laser source is a 830-nm external cavity diode (TBL-6300 from NewFocus) in a Littman-Metcalf (Littman & Metcalf, 1978) configuration. This configuration

allows for the single-mode scanning of laser that uses a diffraction grating as the dispersive element (Liu & Littman, 1981). The rotation of the tuning mirror can provide changes simultaneously in cavity length and diffraction angle that exactly match the requirements needed for continuous single-mode scanning. The tuning mirror can be rotated by a DC motor driven screw and a piezoelectric transducer (PZT). The DC motor makes coarse wavelength change with a minimum wavelength step of 0.02 nm while the PZT is used for micron scale movements which corresponds to sub-angstrom wavelength tuning precision and offers a smooth tuning range of 60 GHz. By keeping the number of waves in the cavity to be constant, this laser provides a 16 nm mod-hop-free tuning range. It has a minimum power of 5 mW and the 50-ms linewidth is less than 300 kHz. The maximum tuning rate of 8 nm/s indicates that this laser can be tuned over the 16 nm range in 2 seconds (NewFocus 2000). Those features make overall a great laser source for MWI and WSI. Although, it has one drawback in that the wavelength error is usually larger than 0.1 nm, limiting the AFR of the MWI.

3.2.2 Interferometer Optics

As shown in Fig. 3.4, linearly polarized light is fed into a polarization maintaining (PM) fiber which feeds a variable beam splitter that splits and inserts the light into object and reference PM fibers. The object light is used to flood illuminate the object with a collimated wave via a parabolic mirror, which in turn collects the scattered object light and sends it to a digital camera. The camera lens along with the parabolic mirror images the object onto the camera detector array. The reference light is combined with the light scattered from the object via a beam splitter to form an inline interferogram detected by the camera and fed to the computer for processing. The

reference wave is set to diverge from a point that is equal distant to that of the focal point of the parabolic mirror. Thus, the reference wave and object wave both appear to diverge from the same plane. The reference PM fiber has extra length to compensate for the free space propagation length of the object wave such that the zero path length difference is slightly above the object surface. The phase of the light is stepped with a computer controlled phase shifter incorporated into the variable beam splitter box. A number of interferograms are acquired, each with its own unique wavelength and step phase. These interferograms are used to form digital holographic images that lead to generating fine resolution 3D shape maps of the object.

3.2.3 Multiple Reference Height Array

As an implementation of MHTIT, an array of calibrated fiducial reflectors in the instrument's field-of-view is used as a multiple reference height calibration device. This array could be a set of flat surfaces composed of an array of height gages or some other calibrated multi-surfaced machined block. We investigate using a linear array of staggered retroreflectors mounted on a superinvar base as the fiducials. The placement of the array is illustrated in Fig. 3.4. The dash line represents the path of the light for multiple reference heights. Note that since the object illumination source and the receiving aperture are displaced from each other, there is typically laser light along one side that is not used and camera pixels along the other side that are not used. Thus by tapping off the otherwise unused light with a mirror and directing it at the array and then using the otherwise unused pixels to view the light from the array via a beam splitter, these unused resources can be utilized.

The reference array, illustrated in Fig. 3.5 (a), is made up of 5 fused silica aluminum coated retroreflectors, evenly distributed linearly, and mounted on a superinvar base. A retroreflector (also known as a corner cube) is a device that an incident wave front is reflected along a vector parallel to but opposite in direction. Because of this unique property, it allows easier alignment than a plane surface mirror. Both fused silica and superinvar have very low thermal expansion coefficients, which allow the array to be insensitive to temperature changes. Each pair of retroreflectors forms a reference cavity, and the OPD between retroreflectors along the optical axis is calibrated as the measurement reference to determine the synthetic wavelengths, as explained in the next section. Fig. 3.5 (b) shows an interferogram obtained from the system for a reference array composed of five retroreflectors. Five retroreflectors are spaced to generate 4 independent OPDs in ascending order of about 0.5 mm, 2.5 mm, 11.1 mm, and 50.1 mm, using the one at the middle as the datum.

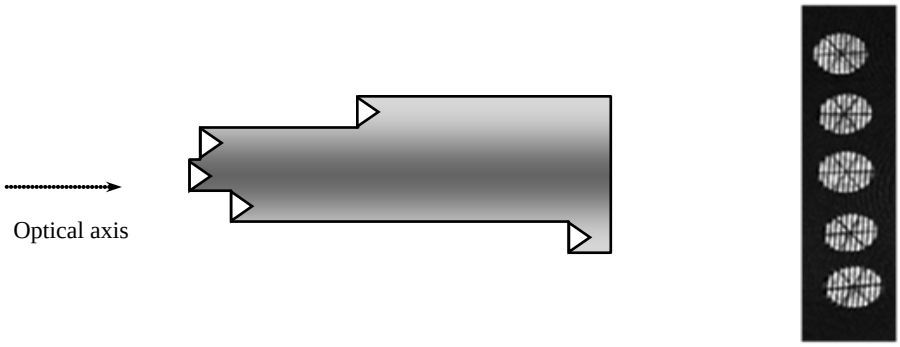

(a) (b)

Fig. 3.5 (a) Reference array, (b) Array interferogram

3.3 Reference Array Calibration

3.3.1 Calibration Principle

The reference array needs to be calibrated accurately to be used as the measurement references. After careful installation and alignment, multiple-wavelength phase shifting interferometry is applied in the ShaPix system for this calibration. A schematic calibration system layout is shown in Fig. 3.6.

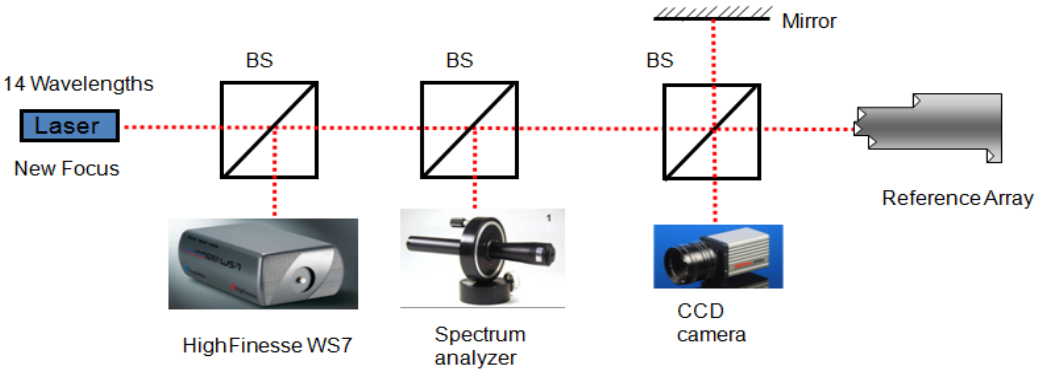

Fig. 3.6 Schematic of calibration system layout

A NewFocus tunable laser is used as the light source. The wavelength measurement is provided by a HighFinesse WS7 wavemeter which provides an absolute accuracy of 60 MHz (HighFinesse, 2011). In addition, a Tropel spectrum analyzer is used as a frequency drifting monitor with a resolution of 3 MHz to make sure the laser frequency is stable during the calibration process at each wavelength. A digital 4 mega-pixel camera is used to capture the interferogram frames. Twelve phase shifted interferograms are recorded at fourteen different wavelengths. The wrapped phase information is calculated by fringe analysis and a phase shifting technique. The data analysis steps, including a phase extraction algorithm and the reference array OPDs measurement will be discussed next.

3.3.2 Interference Fringe Analysis

The need for high accuracy wavefront measuring interferometry techniques has resulted in a variety of data collection and analysis methods. Among them, phase-shifting interferometry (PSI) has been widely applied in a variety of interferometric applications since introduced by Bruning et al. in the 1970's. Interferograms are recorded in the temporal domain while a controlled, relative global phase shift is introduced between reference and object beams. The calculation is performed by the algebraic combination of separately measured intensities with different weights in a way that allows the stationary intensity, the modulated intensity, and the relative phase to be solved separately for each point (Schwider, 1988).

Taking a typical four-frame temporal phase measurement algorithm for example (Creath, 1988), the i^{th} frame interferogram at the camera detector array is proportional to the intensity

$$I_i(x,y) = I_O(x,y) + I_R(x,y) + 2\sqrt{I_O I_R}\cos\{\phi(x,y) + \Delta_i\} \tag{3.14}$$

where $I_o(x, y)$, $I_R(x, y)$ are the intensities of object and reference beam at detector point (x, y), respectively, $2\sqrt{I_O I_R}$ is the modulation of the fringe pattern, $\phi(x, y)$ is the test wavefront phase to be determined, and Δ_i is the applied relative phase shift for the i^{th} exposure. In four-frame technique, the nominal phase-step is $\pi/2$ and the relative phase takes values of 0, $\pi/2$, π, and $3\pi/2$. Using these values, the intensities at each point in frames 1 to 4 are

$$
\begin{aligned}
I_1 &= I_O + I_R + 2\sqrt{I_O I_R}\cos(\phi) \\
I_2 &= I_O + I_R + 2\sqrt{I_O I_R}\cos(\phi + \pi/2) = I_O + I_R - 2\sqrt{I_O I_R}\sin(\phi) \\
I_3 &= I_O + I_R + 2\sqrt{I_O I_R}\cos(\phi + \pi) = I_O + I_R - 2\sqrt{I_O I_R}\cos(\phi) \\
I_4 &= I_O + I_R + 2\sqrt{I_O I_R}\cos(\phi + 3\pi/2) = I_O + I_R + 2\sqrt{I_O I_R}\sin(\phi)
\end{aligned}
\tag{3.15}
$$

from which

$$
\phi = \arctan\left(\frac{I_4 - I_2}{I_1 - I_3}\right) \tag{3.16}
$$

Thus the phases at each point can be determined independently from the neighborhood within a modulo 2π by use of a PSI technique and a 4-quadrant arctangent.

The time-domain phase-shifting techniques provide several advantages over spatial-domain (or Fourier-domain) methods (Takeda et al., 1982) of interference fringe analysis: improved noise immunity, insensitivity to spatial variations in the detector response, high-spatial-frequency resolution, and ease of implementation. The primary source of systematic error in early phase-retrieval methods comes from the requirement that the phase steps be uniform and well characterized. Error minimization for linear phase shift miscalibration has been addressed by several authors (Schwider, 1983; Hariharan, 1987; Surrel 1993; Phillion 1997). Schmidt and Creath (1992) proposed several algorithms for compensating phase shifts with quadratic nonlinearity, and Groot (1995) developed a method to address cubic nonlinearity. Much of the effort in the development of these techniques has been spent to address the errors introduced by the phase-shifting itself. Instead, a different approach measures the individual phase step values during the phase recovery and uses that information to eliminate the measurement errors introduced by phase-step miscalibrations, nonlinearities, and

random step errors (Kinnstaetter, et al., 1988; Han & Kim, 1994; Dobroiu, et al., 1997; Chen, et al., 2000).

The phase retrieval technique applied in this study falls into this latter category, similar to the technique proposed by Goldberg and Bokor in 2001, which includes two steps performed in sequence. Firstly, N global phase steps are generated by varying the output voltage of a piezoelectric transducer (PZT) in the reference arm of the interferometer, and the N global phase positions are determined by Fourier-domain interference fringe analysis (Takeda et al., 1982). The phase positions are then applied as *a priori* information to the least-square method (LSM) of phase retrieval, since the LSM allows the reconstruction of wave-front data when arbitrary global phase-shifting steps are known (Greivenkamp, 1984). By measuring and using the actual phase-step positions during the phase retrieval, we suppress the systematic errors due to nonlinear, irregular phase step increments.

Application of Fourier transform of interference fringe analysis requires the presence of a spatial carrier frequency, or wavefront tilt in the measurement domain. Tilting the array beam splitter allows the control of identically orientated fringes for all the retroreflector images. Fig. 3.7 (a) illustrates the area captured by the camera and the interference existing over the area of the retroreflector face.

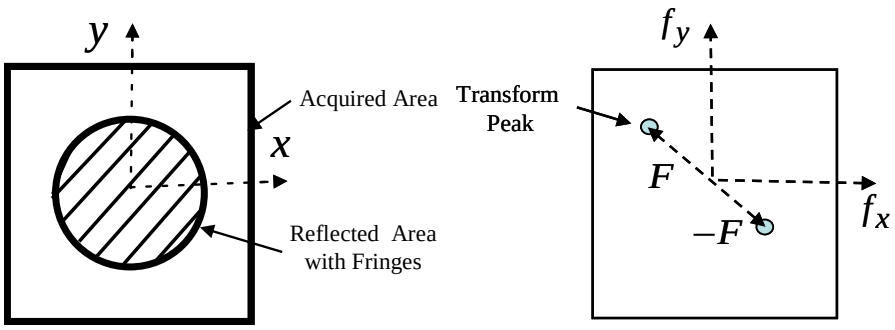

(a) (b)

Fig. 3.7 (a) An illustration of a reflector interferogram, (b) Its Fourier transform

Following the procedure of the widely known Fourier-transform method of interferogram analysis (Takeda, 1982), the fringe phase at the coordinate center can be obtained, which is taken to be the vertex of the retroreflector. We define the relative one way OPD of tilted retroreflector with respect to zero path position as

$$H(x,y) = x\sin(\alpha_x) + y\sin(\alpha_y) + H_o \tag{3.17}$$

Where, α_x and α_y are tilting angles in x and y directions, H_o is the OPD at the coordinate center. The n^{th} step interferogram at the camera detector array is proportional to the intensity

$$I_n = I_O + I_R + 2\sqrt{I_O I_R}\cos\{\tfrac{4\pi}{\lambda}H(x,y) + \Delta_n\} \tag{3.18}$$

Where, I_o, I_R are the intensities of object and reference beams, respectively, λ the free space wavelength of the light and Δ_n is the applied step phase. A weighted signal with the bias removed is generated as

$$S_n = [I_n - I_O - I_R]W(x,y) \tag{3.19}$$

where *W(x,y)* describes the support and applied weighting function that is used for measurement and sidelobe control. Then the spatial Fourier transform of s_n gives the spectrum

$$\begin{aligned} s_n = \Big\{ & \sqrt{I_O I_R}\{w[f_x - \tfrac{1}{\lambda}\sin(\alpha_x), f_y - \tfrac{1}{\lambda}\sin(\alpha_y)]\exp(\tfrac{4\pi i}{\lambda}H_0)\exp(i\Delta_n)\} \\ & + \sqrt{I_O I_R}\{w[f_x + \tfrac{1}{\lambda}\sin(\alpha_x), f_y + \tfrac{1}{\lambda}\sin(\alpha_y)]\exp(-\tfrac{4\pi i}{\lambda}H_0)\exp(-i\Delta_n)\}\Big\} \end{aligned} \tag{3.20}$$

Here, *s* is the Fourier transform (FT) of *S*, f_x and f_y are the FT coordinates corresponding to *x* and *y*, respectively, and $w(f_x, f_y)$ is the FT of the weighting function *W(x,y)*. Fig. 3.7 (b) illustrates that transformed output consists of two peaks associated with the fringe pattern due to the tilted object wave. By examining the complex phase of the FT at s_n where $w(f_x, f_y)$ is maximum, the fringe phase at the coordinate center is obtained.

$$\phi_n = \mathrm{mod}\left((\frac{4\pi}{\lambda}H_0 + \Delta_n), 2\pi \right) \tag{3.21}$$

And the individual step phase Δ_n can be calculated by removing the constant phase term due to H_o and the wavelength λ.

We also note that the spatial frequency of fringes is wavelength dependent so that the stability of the fringes gives us an indication of the system stability (Aleksoff & Yu, 2010). The peak in the FT of the spectrum associated with the fringes has a distance from the origin equal to

$$F = \frac{1}{\lambda}(\sin\alpha_x + \sin\alpha_y) \tag{3.22}$$

If the wavelength changes by $\Delta\lambda$, then the peak moves by

$$\Delta F = \frac{\Delta\lambda}{\lambda^2}(\sin\alpha_x + \sin\alpha_y) \tag{3.23}$$

The relative change in the peak position is given by

$$\frac{\Delta F}{F} = \frac{\Delta \lambda}{\lambda} = \frac{\Delta \nu}{\nu} \tag{3.24}$$

Where $\lambda \nu = c$. This offset can give a coarse measurement of the frequency change, showing the stability of the system laser output.

After N global phase step values are determined from the Fourier domain analysis, the LSM is applied to calculate the wrapped phase information at each point individually based on the intensity distribution of the interferogram and the phase step values. The LSM of phase-shifting analysis is presented in detail in Appendix A.

3.3.3 Data Processing

Once the relative phases at individual points are determined generating a phase map based on the LSM algorithm and parameters, such as the temperature, humidity, pressure and laser wavelengths, have been measured, the data must be processed to produce the result for the OPDs between the coordinate centers of two retroreflectors. The majority of computer processing is devoted to extracting the phase data into a form in which it can be used in the multiple-wavelength analysis, to calculate the OPDs of the reference heights.

The steps of the data processing for reference heights calibration are summarized and illustrated in Fig. 3.8.

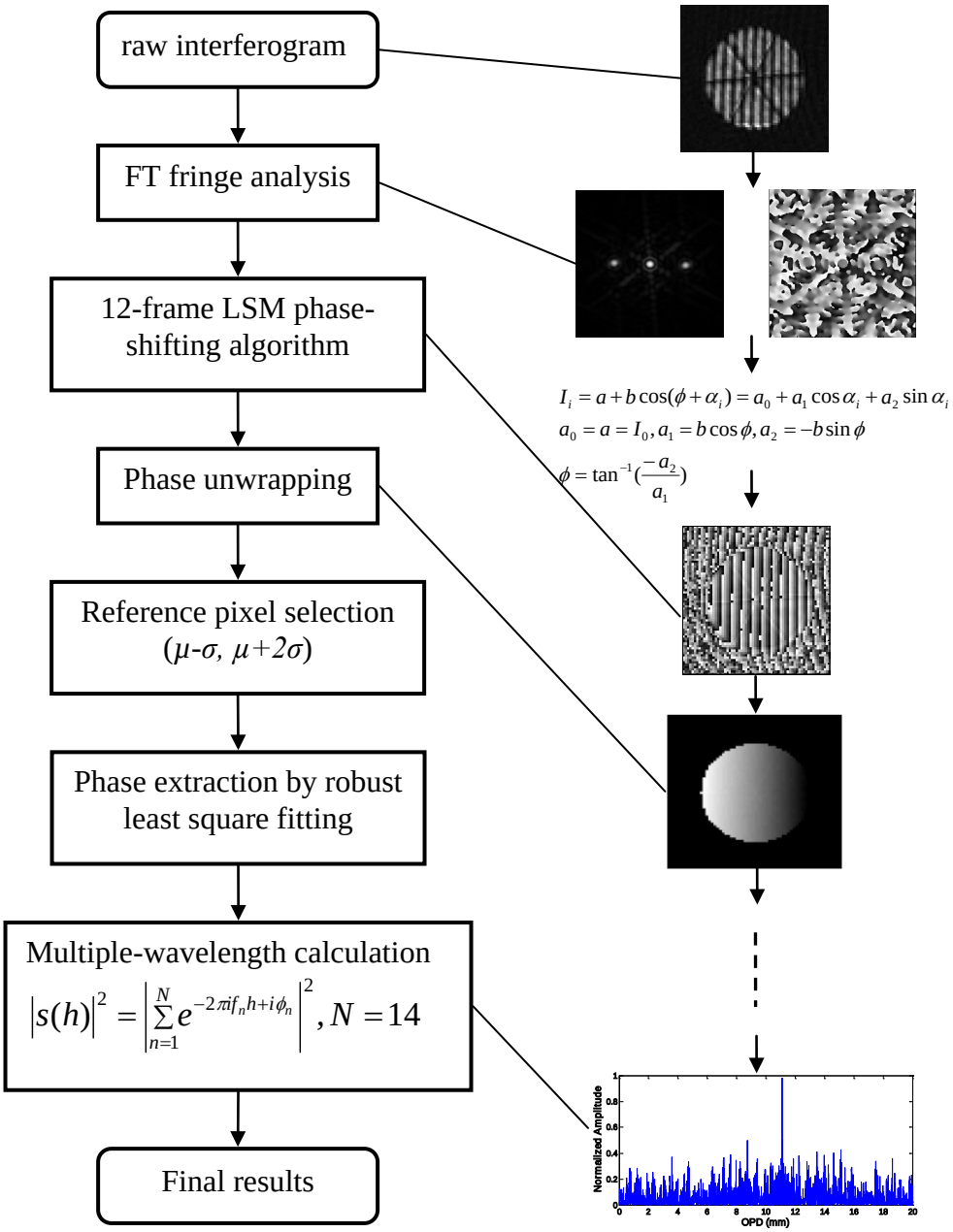

Fig. 3.8 Flow diagram of calibration data processing

Following the data processing diagram, the LSM produces the wrapped phase information of each individual pixel on one reflector surface. In order to reduce the phase measurement error, statistical data analysis methods are used to extract the phase

information at the coordinate center of the retroreflector front surface. The underlying assumption is that the optical reflecting surface of the retroreflector is perfect flat (residual errors are negligible). First, a reliability-guided phase unwrapping algorithm (Su & Chen, 2004) was applied on the data to get unwrapped phase information. Then, we select reference pixels with high modulation value for further analysis in order to reduce the photon noise. Pixels with modulation depth less than certain threshold are removed as background noise. Mean value μ and standard deviation σ of the remaining pixels are computed; those reference pixels must have modulation depth falling into the range (μ-σ, μ+2σ) for all 14 wavelengths. This asymmetric range is determined based on the practical experience and the assumption that the reference pixels have high SNR. Next, a robust least square fitting (LSF) algorithm is applied to the valid reference pixel phase map generating a LSF plane on the tilted wavefronts to remove outliers. Finally, the phase value of the center pixel of the LSF plane chosen from the remaining valid phase map is extracted, and the corresponding phase differences of those center pixels are calculated, which will be used for calibrating the OPDs of the retroreflectors.

The array difference OPDs centered on retroreflectors are then calculated from the FT peak finding algorithm based on the phase and wavelength information, and used in subsequent calculations as the reference height values. Following the above calibration procedure, 4 step fiducial heights are calibrated with approximated height differences of 0.55 mm, 2.475 mm, 11.138 mm, and 50.119 mm. A calibrated relative measurement uncertainty of 2e-6 for the largest height difference is achieved .

3.4 Experiments and Results

Once the reference array is accurately calibrated, a MHTIT measurement can be conducted following the measurement procedure described in Section 3.1.3. The second step is to record the wrapped phases of both reference array and the object at multiple wavelengths. For the reference phase measurement, the same steps are applied as in the calibration stage. For the object phase extraction, a fitting scheme to the sinusoidal variation in intensity with phase change is used to measure the wrapped phase of interest since no fringe pattern can be used to measure the phase step (Lassahn, et al., 1994). Next, wrapped phases of reference array are unwrapped by the MHTIT algorithm, and the object height is determined by the Fourier transform peak finding technique. We conduct several experiments to verify the principle of the MHTIT, and demonstrate the measurement range and accuracy improvement by the use of the MHTIT technique.

3.4.1 Gauge Block Measurements

The measurement of a known step height is presented to verify the measurement range and accuracy improvement applying the MHTIT. A Z-axis stainless steel Glastonbury check master GSG GX-1 was calibrated by the manufacturer and used as the measurement standard shown in Fig. 3.9. This stainless steel gauge block stacks up four 25.4 mm steps so the overall height difference is 101.6 mm.

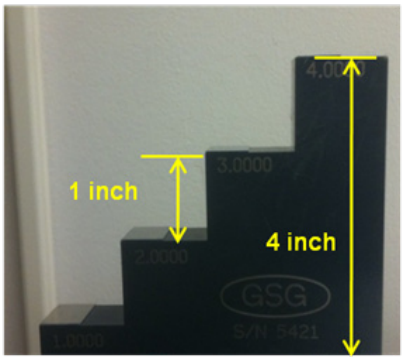

Fig. 3.9 Front view of z-gauge

The typical tuning repeatability of the New Focus tunable laser is ±0.1 nm, which means that a commanded laser wavelength shown on the laser controller may have an absolute wavelength error up to 0.1 nm. Then the MWI measuring system can only measure up to 5 mm height differentials with one micron accuracy (Coherix, 2011). If a 25.4-mm z-gauge block is measured, noise amplification due to inaccurate wavelength information will cause the sidelobe to become the main peak in the peak finding algorithm leading to large measurement error. As shown in Fig. 3.10, the peak position gives a measured height of 29.1 mm while the actual height is 25.4 mm.

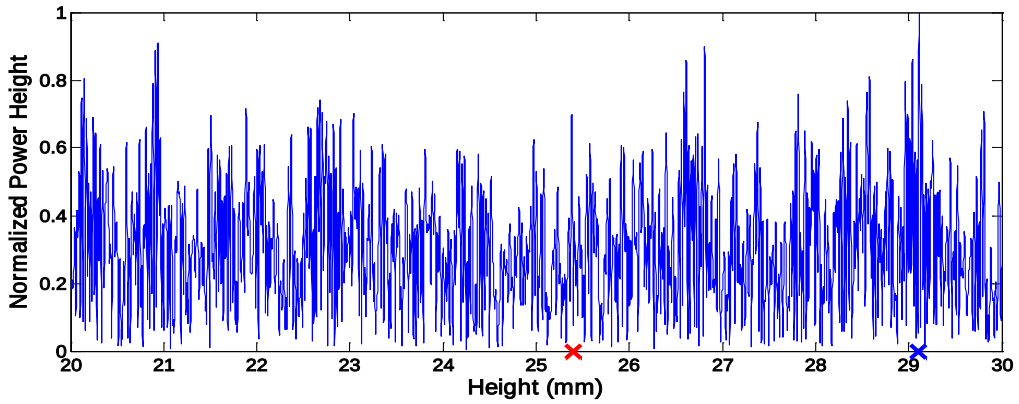

Fig. 3.10 An example plot of power height response function measuring a 25.4-mm gauge block without applying the MHTIT.

By applying the proposed MHTIT with calibrated fiducial OPDs, the gauge block was successfully measured. The experimental result is shown in Table 3.2.

Table 3.2 Stainless Steel Gauge Block Measurement Results

Specification[a]	Mean (mm)	STD (μm)
25.4023 mm ± 0.4 μm	25.4030	0.2
50.8015 mm ± 0.4 μm	50.8019	0.2
76.2025 mm ± 0.4 μm	76.2024	0.2
101.6015 mm ± 0.4 μm	101.6018	0.2

[a]Specification is calibrated in 20^{o} Celsius, 45% humidity.
Measurement is conducted in room temperature 20^{o} Celsius.

Where, the average distance between two separated surfaces among 100×100 pixels area are given as the mean value and STD represents the standard deviation of 10000 independent measurements. As shown in Table 3.2, a large range of height measurement is achieved successfully by applying the MHTIT with sub-micron accuracy. The system measurement range is increased from 5 mm to over 100 mm without knowing accurate wavelength information.

3.4.2 Industrial Part Measurements

Some 3-D images with multiple surfaces obtained with this method are presented in this section. The images demonstrate the successful applications of the MHTIT technique in workshop environments. The first set of images shown in Fig. 3.11 represents a study of valve body for an automatic transmission. The application is to measure the surface profile, and distance between two discontinuous surfaces. Fig. 3.11 (a) shows the photograph of a valve body. Fig. 3.11 (b) shows the 3D measurement results, where the perspective display represents the height or distance variation of two

surfaces. Another example is a pump housing part shown in Fig. 3.12. By applying the MHTIT, the distance measurement capability between two discontinuous surfaces is improved.

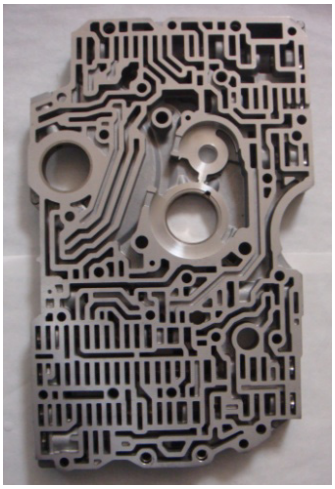

(a)

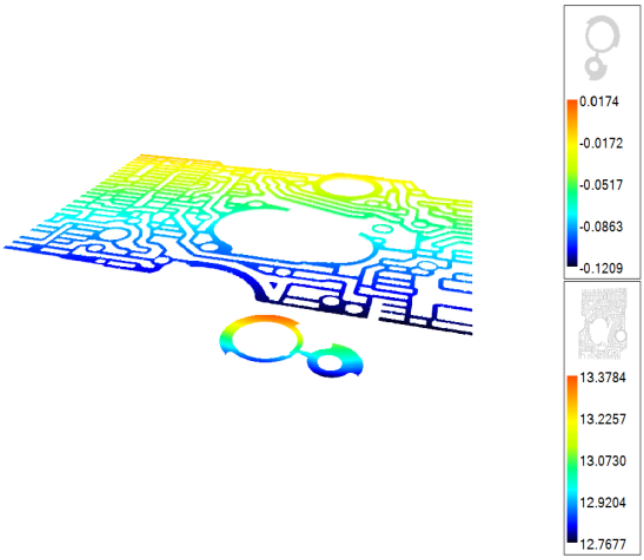

(b)

Fig. 3.11 (a) Photograph of an automotive valve body, (b) 3D mesurement result

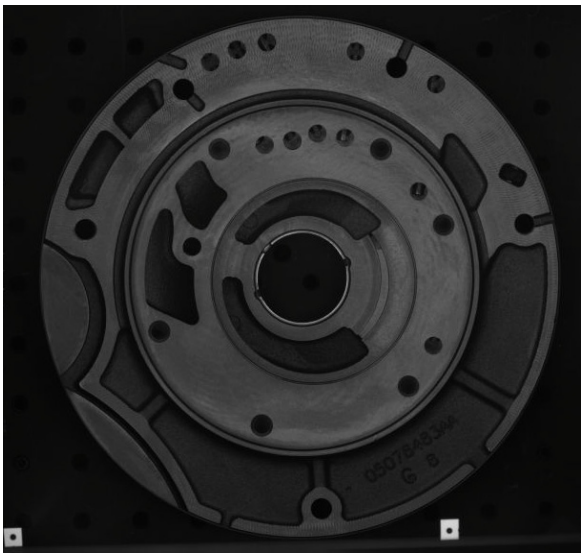

(a)

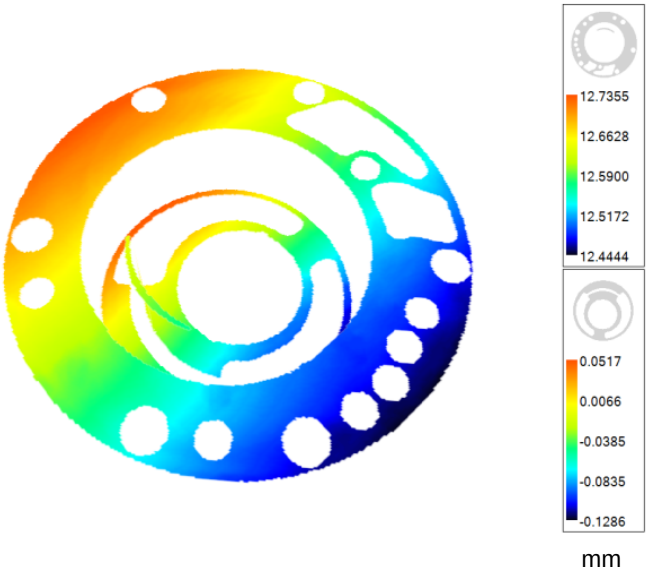

(b)

Fig. 3.12 (a) Photograph of an automotive pump housing, (b) 3D mesurement result

3.5 Summary and Conclusions

In this chapter, a multiple height-transfer interferometric technique (MHTIT) has been proposed that increases the absolute distance measurement ambiguity-free-range of an interferometric measuring system. By making use of multiple accurately calibrated reference heights, this technique relaxes the requirement of knowing accurate wavelength information for multiple wavelength interferometry while maintaining its advantages. A reference array is built and installed in the measuring system, which consists of multiple retroreflectors mounted on a superinvar base. The optical path differences (OPDs) between retroreflectors along the optical axis are calibrated in the measuring system and used as measurement references. Synthetic wavelengths used in classical metrology system are instead replaced by the ratio of reference OPDs and corresponding phase differences. This new technique reduces the sensitivity to certain types of noise, allowing it to be more suitable for full surface measurements with large height difference in industrial environments. Improvement for absolute distance measurement capabilities by use of this technique was demonstrated by measuring a known height gauge block. The experimental results showed increased measurement range of over 100 mm with sub-micron accuracy. 3D measurement results of some industrial parts were also presented, showing the successful applications of the MHTIT in workshop environment. This improved extension for multiple wavelength interferometry can benefit precision manufacturing, improving product quality and reducing warranty cost.

CHAPTER 4
MEASUREMENT UNCERTAINTY ANALYSIS

The multiple height-transfer interferometric technique has been developed based on the concepts of multiple-wavelength interferometry and wavelength-scanning interferometry to increase the absolute distance measurement capability of a metrology system. Its feasibility and applicability has been demonstrated by measuring both a gauge block and industrial parts. In this chapter, we summarize the measurement results, present an uncertainty analysis, analyze the primary sources of uncertainties limiting the performance of this technique, and discuss how errors can be minimized.

4.1 System Performance

The measurements of a known step height are presented to verify measurement performance of the multiple height-transfer interferometric technique (MHTIT). A Z-axis Glastonbury check master GSG GX-1 was calibrated by the manufacturer to be 50.8015±0.0004 mm with a confidence level more than 95% at 20^{o} C, 45% humidity. The experiment applying the MHTIT was conducted in a laboratory whose temperature and relative humidity were regulated within 20 ± 0.1^{o}C and 50±10%, respectively. Fig. 4.1 shows the results of 400 repeated measurements over about 10 hours. The distance between two surfaces of a 50.8-mm step height was measured to be 50.8019±0.00031 mm at a confidence level of 95% (2σ), in agreement with the calibration

specification (the dashed line) and resulting in a physical height measurement precision of 6.2 ppm. Detailed uncertainty analysis will be discussed in the next section.

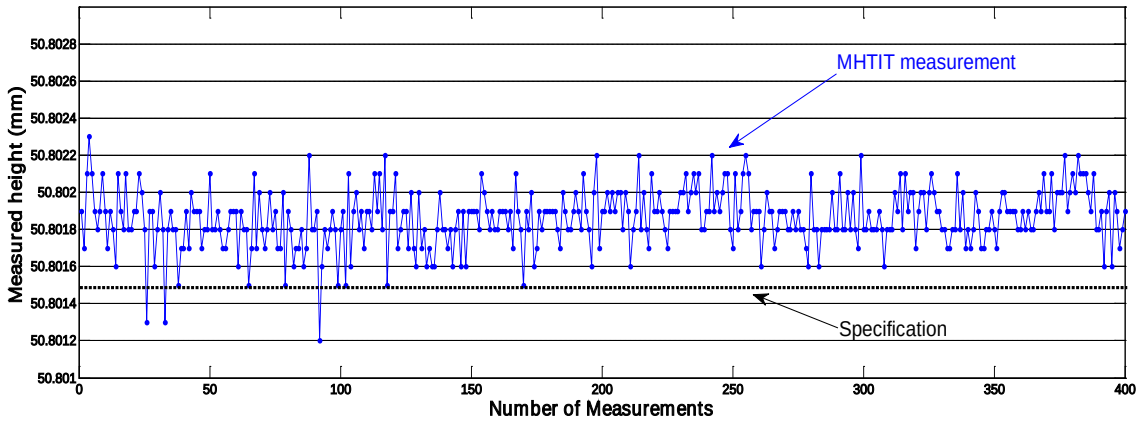

Fig. 4.1 Measurements of a 50.8-mm step height

4.2 Measurement Uncertainty Analysis

The MHTIT applies multiple-wavelength interferometry (MWI) to generate variable synthetic wavelengths from the beating of two or more wavelengths. The synthetic wavelengths are determined from a reference interferometer and the corresponding phase differences, which is analogous to synthetic wavelength measurement process in wavelength-scanning interferometry (WSI). Conventional WSI obtains the phase differences by counting the fringes passing in two separate interferometers, a reference interferometer of a known length h_{ref} and a measuring interferometer h_{meas} during the wavelength sweep. If h_{ref} and h_{meas} are defined as the one-way optical path difference (OPD) in the two arms of the reference and measurement interferometers, and the observed changes in the phase of the optical

interference are defined as $\Delta\Phi_{meas}$ and $\Delta\Phi_{ref}$, then the unknown length of the measuring interferometer can be determined from

$$h_{meas} = h_{ref} \frac{\Delta\Phi_{meas}}{\Delta\Phi_{ref}} \tag{4.1}$$

The MHTIT utilizes the same fundamental measurement principle. Following the *Guide to the Expression of Uncertainty in Measurement (GUM)*, published by ISO in 1995, the standard uncertainty of h_{meas}, denoted by $U(h_m)$, is obtained by appropriately combining the standard uncertainties of the other inputs, which is given by

$$\begin{aligned} U(h_m) &= \left\{ \sum_i [\frac{\partial h_m}{\partial X_i} \cdot U(X_i)]^2 \right\}^{1/2} \\ &= h_m \left[\left(\frac{U(h_r)}{h_r} \right)^2 + \left(\frac{U(\Delta\Phi_r)}{\Delta\Phi_r} \right)^2 + \left(\frac{U(\Delta\Phi_m)}{\Delta\Phi_m} \right)^2 \right]^{1/2} \end{aligned} \tag{4.2}$$

Three uncertainty components are related to reference height h_r, reference phase shift $\Delta\Phi_r$ and measurement phase shift $\Delta\Phi_m$. Since the phase shift $\Delta\Phi$ can be expressed by h and synthetic wavelength Λ according to Eq. (3.3), the expression for $U(h_m)$ is

$$\begin{aligned} U(h_m) &= h_m \left[\left(\frac{U(h_r)}{h_r} \right)^2 + \left(\frac{U(\Delta\Phi_r)}{4\pi h_r} \Lambda \right)^2 + \left(\frac{U(\Delta\Phi_m)}{4\pi h_m} \Lambda \right)^2 \right]^{1/2} \\ &= \left[h_m{}^2 \left(\frac{U(h_r)}{h_r} \right)^2 + h_m{}^2 \left(\frac{U(\Delta\Phi_r)}{4\pi h_r \Delta\lambda} \lambda^2 \right)^2 + \left(\frac{U(\Delta\Phi_m)}{4\pi\Delta\lambda} \lambda^2 \right)^2 \right]^{1/2} \end{aligned} \tag{4.3}$$

Where, $\Delta\lambda$ is the applied wavelength difference, and λ is the center wavelength. It can be seen that first two terms are object height dependent and the other uncertainty term is inherent to the measurement, which will present an error even if a 'zero-height' object is measured. Another observation in the second term is that h_r is inversely proportional to the phase measurement uncertainty of the reference interferometer, which explains

the necessity of applying a large reference height to reduce the reference phase uncertainty. Also shown in the equation is that the uncertainty in the phase measurement will be amplified by $\lambda/\Delta\lambda$ times, which is the characteristic of WSI or MWI.

The first term of the uncertainty with respect to h_r is determined by the calibration and during the use of the reference interferometer, by its stability. The calibration of the longest reference height using WMI gives a relative uncertainty $U(h_r)/h_r$ of 2×10^{-6} (discussed in Chapter 3), thus leading to an uncertainty of 0.1 μm for 50.8 mm measurement OPD h_m. The variation in the reference OPD can arise from both purely mechanical sources or from optical effects. Although thermal expansion of superinvar base introduces only 5 nm per degree C for the longest reference height difference of 50 mm, about 70 nm additional optical path variation due to refractive index change is estimated, which will be discussed in the next section. Furthermore, the geometry of multiple reference heights is somewhat prone to the alignment error, also explained in the next section. We observed a day-to-day variation in the OPD of reference arm on the order of $\Delta h/h = 1.4\times10^{-6}$. Thus the total relative uncertainty in reference height h_r is 3.4×10^{-6} by combining two uncertainty aspects (calibration uncertainty and day-to-day variation), corresponding to a 0.17 μm uncertainty for a 50.8 mm OPD.

As shown in Eq. (4.3), the second uncertainty term, the uncertainty in reference phase measurement $U(\Delta\Phi_r)$, depends on the uncertainties of the phase retrieval technique and the reference height h_r. The phase uncertainty is examined by the use of a spatial fringe analysis method to measure the phase difference between two

retroreflectors, as discussed in the next section. The variation of the phase difference indicates the phase measurement uncertainty. Fig. 4.2 shows a normal variation in the interference phase over 5 seconds as the wavelength is kept constant. In this study, a measurement involves a discrete wavelength scan, where the data collection takes less than 1 second at each wavelength. Hence, during a measurement, the reference phase error at each wavelength is approximately $\pm 2^{o}$ (1σ). As h_r is 50 mm, the uncertainty in reference phase corresponding to the second term in Eq. (4.3) contributes about 0.1 μm to the final measurement uncertainty.

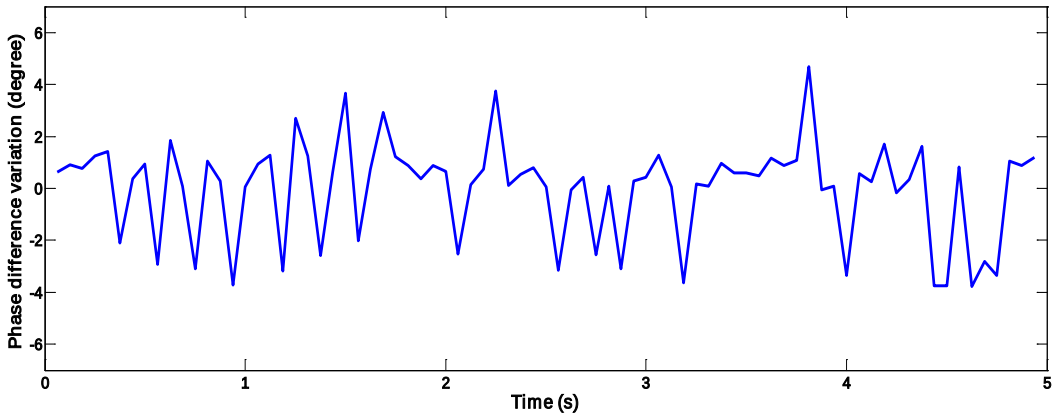

Fig. 4.2 Measured variation of the interference phase of reference interferometer

The same experiment was conducted to check the phase variation on the measured step height surface, corresponding to the third uncertainty term in Eq. (4.3). The standard deviation of phase variation $U(\Delta\Phi_m)$ is approximately $\pm 3^{o}$, contributing about a 0.15 μm uncertainty in the measurement. It is greater than the reference phase variation, presumably because the measured step height is not placed in a sealed environment so that significant air turbulence exists in the measurement arm. Also, more phase variation from wavelength to wavelength is expected for the measurement of a ground surface finish compared to that of a mirror surface.

As explained above, the uncertainties from three terms in Eq. (4.3) contribute approximately 0.1 μm to 0.17 μm to the final measurement uncertainty. By taking the positive square root of the combined variance from these three terms, $U(h_m)$ is estimated to be 0.25 μm. With a coverage factor of 1.96 corresponding to the confidence level of 95%, the final uncertainty estimate is 0.5 μm, slightly overestimating the observed 0.31 μm uncertainty (2σ) at 50.8 mm.

In general, the final measurement uncertainty may come from many sources. The following sections thus provide discussions of sources of errors that may be expected to be important in a MHTIT measuring system and indicate possible ways to minimize the errors.

4.3 Discussion of Error Sources

4.3.1 General Considerations

The data capturing of the MHTIT measurement is similar to WSI measurements and phase shifting MWI measurements, since the unknown length is determined from the ratio of total phase shift observed while tuning the laser. But the MHTIT involves a unique phase unwrapping procedure using multiple reference heights. To understand the system measurement uncertainties, the sources of errors must be taken into account.

First, the MHTIT requires the shortest reference height to unwrap the phase shift and the longest reference height to provide the best measurement accuracy. The robustness of phase unwrapping relates to the number and spacing of multiple reference heights and the measuring system signal-to-noise ratio (SNR). Fewer reference heights

are needed if the SNR is higher. In the presence of system noises, more reference heights offer robust phase unwrapping and reduce the sensitivity to certain noises but add cost and system complexity. An optimal selection of number and spacing is desirable to be tolerant to system noises. A numerical simulation using the Monte-Carlo method is presented in the following section to discuss how to select multiple reference height spacing.

Second, one of the advantages of applying the MHTIT in an interferometric measuring system is the ability to achieve high sample density and large field of view measurements for industrial parts. Correspondingly, expanding the laser beam results in long optical path employed in the system. Hence, OPD variation due to the refractive index change can be significant due to the long optical path of the measurement system. We need to consider the long term OPD variation caused by thermal gradient variation of the optical path for the reference height, which is presented in Section 4.3.3.

Third, the Fourier transform method is applied to extract the phase step from the fringe pattern on the retroreflector surface. Spectrum leakage in the Fourier domain will introduce additional phase measurement error. It is observed that the orientation of a retroreflector with respect to the direction of the interference pattern, edge effects and system SNR all impact the phase measurement accuracy. Therefore, the technique of applying a window function and rotation of the retroreflector is described to minimize this error in Section 4.3.4.

Last, but not least, alignment errors have to be considered in the MHTIT measurement because long term stability of reference heights relates to measurement

reliability. Significant OPD variation will occur as a result of alignment instability. We then propose a rotation invariant module and its working principle to compensate for possible alignment errors in Section 4.3.5.

4.3.2 Numerical Simulation of Multiple Reference Height Spacing

Generally, the optimum design of array spacing depends on the system noise distribution, absolute distance measurement accuracy and reliability requirement. We conduct numerical simulation using the Monte-Carlo method to assess the impact of measurement noises on optimal array spacing geometry based on a given system noise model. Four different multiple height spacing designs are generated to be the simulation inputs. A system noise model including phase measurement errors and array spacing errors is built based on the three uncertainty terms in Eq. (4.3). The object height to be measured is 50.8 mm. After applying the MHTIT for 1000 simulation runs, the standard deviation and the outlier rate are computed to compare the performance of each design. Here, an outlier is defined as a measurement result which has more than 100 microns absolute error compared with the actual object height. The outlier occurs when measurement noise causes the sidelobes to increase relative to the mainlobe (peak) and even become a false peak with a higher value than the correct mainlobe peak in the peak finding algorithm.

First, a proper shortest reference height needs to be determined to avoid the phase ambiguity caused by the wavelength difference uncertainty. Based on Eq. (3.3), if the wavelength difference is $\Delta\lambda$, its uncertainty $\pm\varepsilon_\lambda$ and the center wavelength λ, the phase difference uncertainty $\pm\varepsilon_\phi$ induced by the wavelength difference uncertainty is

$$\varepsilon_\phi = \frac{\Delta\lambda + \varepsilon_\lambda}{\lambda^2} 4\pi h_1 - \frac{\Delta\lambda_\lambda}{\lambda^2} 4\pi h_1 = \frac{\varepsilon_\lambda}{\lambda^2} 4\pi h_1 \tag{4.4}$$

In order to avoid the 2π phase ambiguity, that is, ε_ϕ is smaller than π (or $-\varepsilon_\phi > -\pi$), the shortest reference height h_1 must satisfy the following equation:

$$h_1 \le \frac{\lambda^2}{4\varepsilon_\lambda} \tag{4.5}$$

The maximum wavelength difference error of the laser sources employed in this work that ranges over a 15 nm bandwidth is ±0.3 nm based on the observed data, so a h_1 smaller than 0.55 mm for 830 nm λ is required for the next step phase unwrapping based on Eq. (4.5).

From practical application, we consider only the case of five fused silica retroreflectors that are laterally spaced 10 mm apart, which generates four independent height differences. Many properties and techniques for finding useful array distributions have been established in the literature for other applications (Towers 2003, Falaggis 2009). Phase unwrapping in the MHTIT includes an iterative calculation algorithm, which allows the phase ambiguity being addressed and the corresponding synthetic wavelength being corrected to a new value with a smaller uncertainty than the preceding stage. Therefore, in order to achieve the maximum robustness in overall phase unwrapping for reference heights, the robustness of phase unwrapping at each stage must be equal (assuming the phase noises are the same for all steps) meaning that a constant ratio between successive reference heights is desirable.

We now evaluate the measurement performance of four different designs laid out in Table 4.1, where the height differences form a geometric sequence. As shown in

Fig. 4.3, they all have the same shorted OPD h_1 but varying in the common ratio of the geometric sequence from 3 to 5.

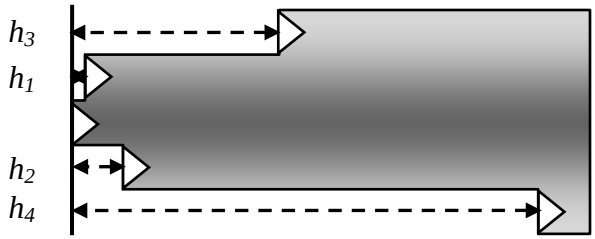

Fig. 4.3 Multiple height spacing

Table 4.1 OPDs (mm) for Different 5-Element Array Designs

	Design 1	**Design 2**	**Design 3**	**Design 4**
h_1 (mm)	0.55	0.55	0.55	0.55
h_2 (mm)	1.65	2.2	2.475	2.75
h_3 (mm)	4.95	8.8	11.138	13.75
h_4 (mm)	14.85	35.2	50.119	68.75
Ratio	3	4	4.5	5

Next, a hybrid error model is added into the measurement input, which consists of array spacing errors and additive phase measurement errors following the uncertainty analysis in the previous section. For the phase error model, considering all the retroreflectors are placed in a relatively uniform environment, we add a Gaussian noise with a zero mean and 0.2 radian standard deviation for all the reference heights in the model. The measurement phase error is estimated to be larger than the reference phase error, so a Gaussian noise model with zero mean and 0.5 radian standard deviation is generated. For the array spacing error model, in a practical optical system, we have to consider both length-proportional scale error due to calibration and thermal expansion and also potential mechanical movement which is independent of length. In this simulation, a uniform distribution of spacing error in the range of [-3, 3] μm is added

into the model. Note that we choose the amplitudes of errors based on the real experiment observations, but they are intentionally overestimated than expected in real experiments in order to better compare the performance of different spacing designs. The system input and noise models are shown in Table 4.2.

Finally, 1000 simulations using the MHTIT algorithm were conducted for calculating the object height. As the ratio of the geometric series increases, the longest reference height increases so its relative uncertainty decreases since the absolute spacing error remains the same. Increasing the ratio can help reduce the measurement uncertainty but will be more susceptible to phase noises leading to unreliable phase unwrapping and more outliers in the measurement results. On the other hand, a smaller constant ratio that leads to a shorter reference height can be more tolerant to phase noises giving robust phase unwrapping, but the larger relative uncertainty in reference height also causes more outliers due to high sidelobes in the peak finding algorithm. Hence the array spacing should be selected in order to optimize the overall measurement accuracy and robustness. The simulation results of the 4 designs are shown in Fig. 4.4.

Table 4.2 System Inputs and Noise Models

λ (wavelength input)	14 λ at 830 nm over 15 nm range
h (object height to be measured)	50.8 mm
ε_{hr} (reference height errors)	[-3, 3] μm (uniform)
$\varepsilon_{\phi r}$ (reference phase errors)	0.2 radian (normal)
ε_{ϕ} (measurement phase errors)	0.5 radian (normal)

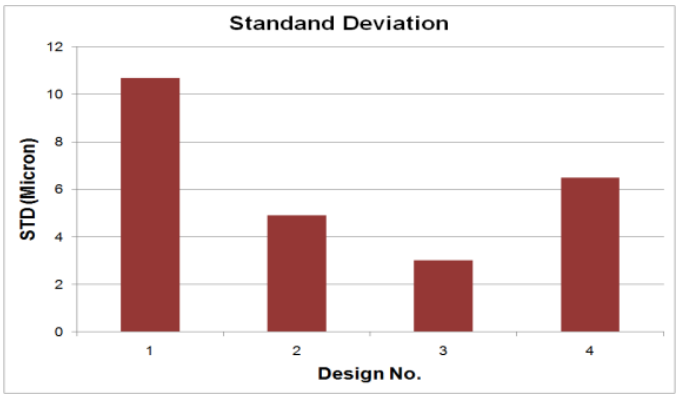

(a)

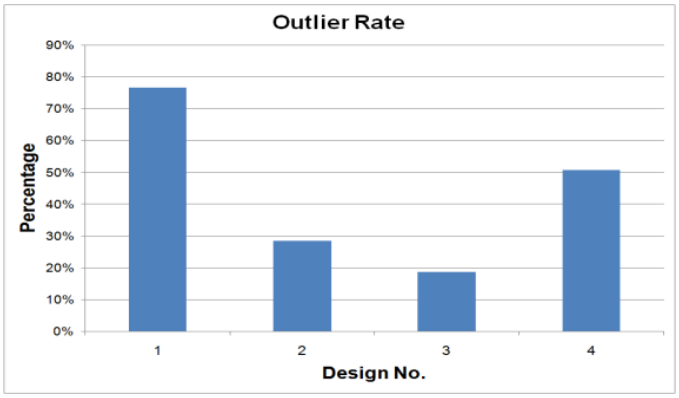

(b)

Fig. 4.4 (a) Standard deviation simulation results, (b) Outlier rate simulation results

Fig. 4.4 (a) shows the standard deviation of the simulation results for 4 designs representing the measurement uncertainty, and Fig. 4.4 (b) gives the outlier rate comparison between designs indicating the reliability of the measurement. It is shown in the plots that the minimum standard deviation and outlier rate occurs for design 3 which a common ratio of 4.5. Following the above discussions, the reference height uncertainty contribution dominates the errors for the smaller ratio in designs 1 and 2, and unreliable phase unwrapping dominates for the larger ratio in design 4. Design 3

thus renders the best measurement performance under the given system noise model. It shows the importance of picking the correct geometric ratio.

4.3.3 Near Common Optical Path Difference

The uncertainty of a near common optical path difference is generally neglected in many interferometric systems if the environment is well controlled and the refractive index difference is small. But it can be a significant factor in our system because it is not feasible to strictly control the environment for our system with a large cavity size, which impacts the long term stability of the reference interferometer. We now consider two closely placed retroreflectors, in a near common path configuration as shown in Fig. 4.5. The optical path difference (OPD) between the two reflectors is calibrated and will be used as the measurement reference in this study.

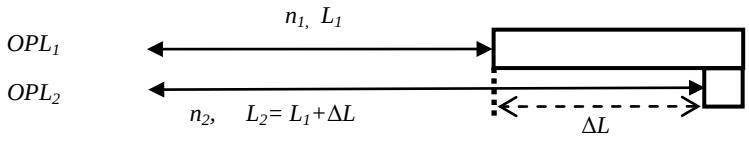

Fig. 4.5 Near common optical path configuration

$$\begin{aligned} OPD &= OPL_1 - OPL_2 \\ &= n_2(L_1 + \Delta L) - n_1 L_1 = \Delta n L_1 + n_2 \Delta L \end{aligned} \tag{4.6}$$

Where, n_1, n_2 are the refractive indices of air along two optical paths, $\Delta n = n_2 - n_1$, $OPL_1 = n_1 L_1$ and $OPL_2 = n_2 L_2$ are the two optical path lengths. If the L_1 is small, OPD variation from the first term is negligible and the main contribution lies in the variation of the second term, which is the case for many interferometers. But in the ShaPix system layout, L_1 from source to camera focus is over 3 m in order to accommodate a large field of view, as shown in Fig. 4.6.

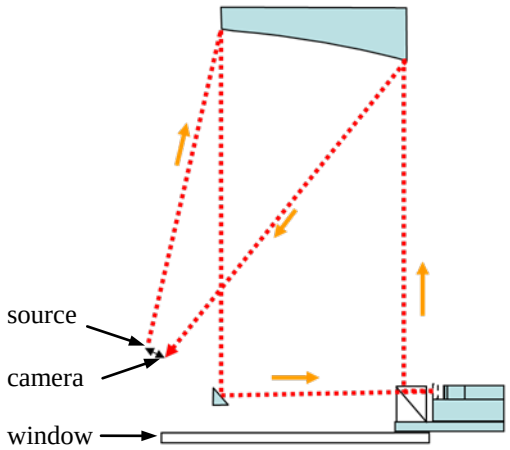

Fig. 4.6 Schematic of the system OPL layout

Table 4.3 gives OPD change caused by change in the index of refractive of air due to temperature variation.

Table 4.3 OPD Change Due to Temperature Uncertainty

Temperature uncertainty	**Change in the refractive index of air**	**OPD difference for 3000mm OPL**
±1°C	1 ppm	3000 nm
±0.1°C	0.1 ppm	300 nm
±0.01°C	0.01 ppm	30 nm

As shown in Table 4.3, the long OPL is susceptible to environmental disturbances and makes it difficult to maintain stable OPDs. Keep in mind that the first term in Eq. (4.6) will vary only if the air refractive index difference along the two paths changes. It means the gradient of the air refractive index should be constant to keep the OPD stable. To strictly evaluate the air refractive index variation along two optical paths inside system cavity, sensors need to be installed along the optical path. In practice, we monitored the temperature variation at two locations along two optical paths by placing two pairs of temperature probes (GEC instruments-Model S8TH accuracy of 10^{-3} °C) 50

mm away from each other. The thermal gradient shows maximum 0.02^{o} C variation at two locations in 24 hours, which contributes 60 nm OPD variation to the first term in Eq. (4.6) due to the refractive index change calculated from the updated Edlén equation (Birch & Downs, 1994). We also assessed OPD variation due to the second term in Eq. (4.6). By measuring the temperature difference along a 50 mm optical path, 0.1^{o} C difference was observed and resulted in 5 nm uncertainty. The uncertainty from the first term is dominant and not length dependent. In order to minimize this error, adding a fixed-wavelength laser to correct for variations in the optical path would help. Another possible way is to adopt multiple Fabry-Perot cavities as measurement references (Vaughan, 1989). The common path design of Fabry-Perot cavity eliminates the first term in Eq. (4.6), but they would complicate the system and add additional costs.

4.3.4 Phase Retrieval Method

Time-domain phase-shifting techniques have been widely used due to its advantages over spatial-domain methods, including improved noise immunity, high-spatial-frequency resolution and ease of implementation. Its primary source of systematic error comes from the requirement that the phase steps be uniform. In this study, the phase measurement of the reference interferometers uses the least-square method (LSM) of phase-shifting analysis (Greivenkamp, 1984). The LSM allows the reconstruction of wave-front data when arbitrary global phase-shifting steps are known. N global phase positions are determined by the Fourier domain fringe analysis to correct the nonlinear, irregular phase step increments due to the piezoelectric transducer (PZT) in the measuring system.

As discussed in Chapter 3, tilting the array beam-splitter introduces additional straight fringes for all the retroreflector images, which corresponds to the carrier frequency in the Fourier domain. Following the procedure of Fourier-transform interferogram analysis (Takeda 1982), the fringe phases at the coordinate centers of the retroreflectors for each phase step can be obtained, which will then be used to determine the relative phase for each wavelength by the least square method.

In the processing, we found several aspects that could impact the step phase measurement accuracy such as the orientation of a retroreflector, modulation depth (defined by $2\sqrt{I_O I_R}$ in Eq. (3.17)) and the use of the windowing function. Observation of the image of a retroreflector shows three lines made by the intersecting reflection faces. We denote these lines as cross hairs. A series of simulated fringe patterns were then generated given the same phase input but with different retroreflector orientations and different modulation depths. By applying the discussed Fourier transform method with windowing functions, we analyzed simulation results and presented the best way to minimize potential phase errors.

The first case simulated is where one cross hair of the retroreflector is aligned parallel the fringes, which have a high modulation depth of 0.95. The image shown in Fig. 4.7 (a) consists of 256 by 256 samples spaced at 150 microns and the retroreflector face is 6 mm in diameter. Fig. 4.7 (b) is the logarithm display of the Fourier transform (FT) magnitude of the first image and Fig. 4.7 (c) shows the phase map of the transform as a gray scale display. The FT coordinates are centered on the retroreflector cross hairs in the image. The phase is measured at the peak on the left in the third image, which

gives about 127.19 degrees for an input of 123 degrees, i.e., an error of 4.19 degrees. The contention is that much of this error comes from the influence of the extent of the point spread function associated with the peak at the center and at the conjugate peak on the right. It is seen that the particular orientation of the fringes and cross hairs give high sidelobes at the peak of the interest. Rotation of the fringes or cross hairs alleviates this problem.

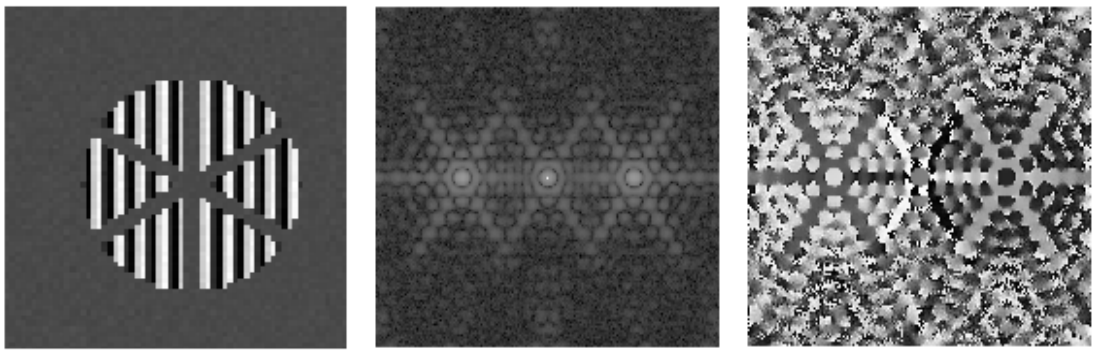

(a) (b) (c)

Fig. 4.7 (a) Simulated fringe pattern, (b) Log display of FT magnitude, (c) Phase map of FT

Therefore, a second fringe pattern is generated as shown in Fig. 4.8 (a), where the parameters are the same with the first simulated fringe except that the retroreflector has been rotated so that in the FT domain the prominent sidelobes do not overlap. The result is considerably better, giving a phase error of only 0.43 degree. Another case shown in Fig. 4.8 (b) is non-rotated retroreflector but with much low modulation of 0.14. The phase error of 4.08 in this case is not much changed from the high modulation case. And Fig. 4.8 (c) is the rotated version of the low modulation case, showing some improvement in the error, but the photon noise influences the results significantly. With the same parameters as in the previous case, but with a Gaussian weighting of 3 mm standard deviation shown in Fig. 4.8 (d) the error has been reduced from 2.59 degrees to

0.10 degrees. Fig. 4.8 (e) shows that simulation for the low modulation case and non-rotation. In this case, the Gaussian filter alone does not help significantly, since the change is from 4.08 degrees to 3.59 degrees. This indicates that the high side lobes dominate in causing the error.

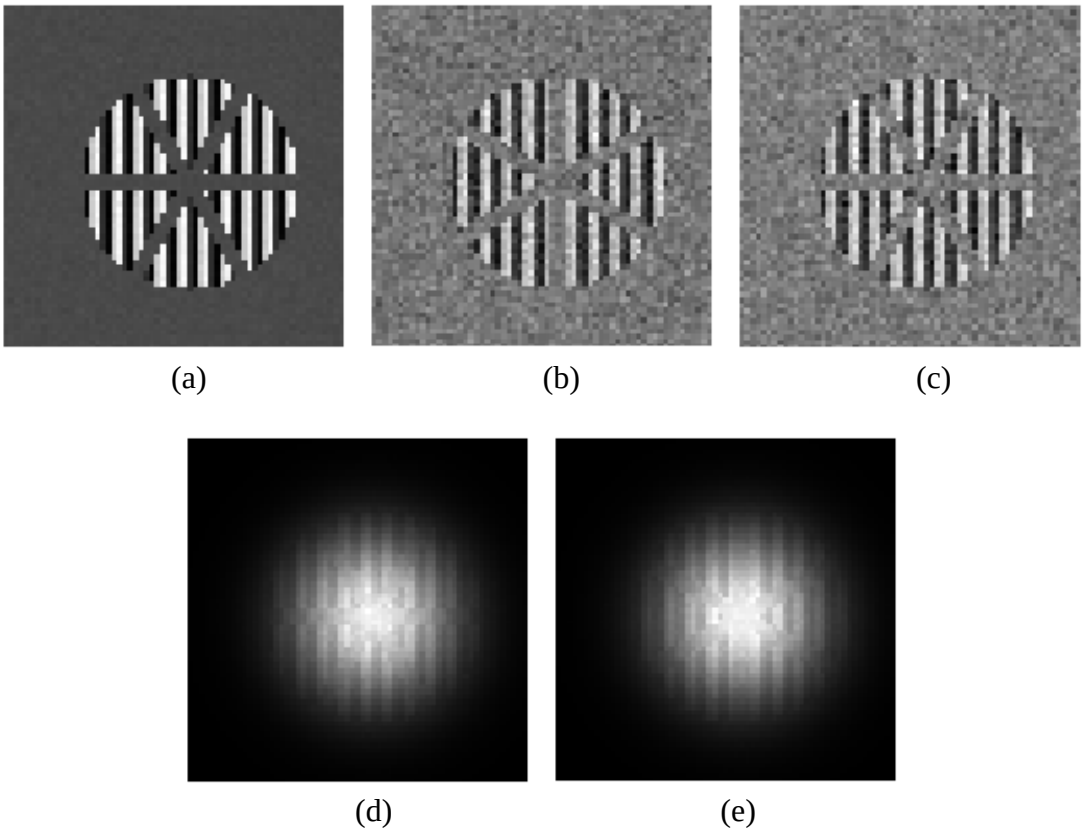

Fig. 4.8 (a) Rotated, high modulation, no filter (b) Non-rotated, low modulation, no filter (c) Rotated, low modulation, no filter, (d) Rotated, low modulation, Gaussian filter (e) Non-rotated, low modulation, Gaussian filter

To sum up, it was shown that the phase measurement at the modulation peak can be improved by orientating the retroreflector such that the cross hairs diffraction patterns from the conjugate modulation peak and bias peak do not contaminate the phase of the modulation peak being measured. Also, Gaussian weighting the image

which primarily includes energy from the fringe area improves the phase measurement, especially in low SNR situations.

4.3.5 Alignment Errors

The alignment error in a Michelson interferometer is often described as a cosine error depending on the angle between the laser beam and the direction of retroreflector (Stone & Stejskal, 1998). This cosine error is not significant in our system since we calibrate the reference height in the same direction as it is employed for measurement. But a significant error will occur if the direction of the incoming laser beam can vary or a common wavefront tilt exists. The problem can best be formulated by the use of an appropriate definition of the optical axis of the interferometer shown in Fig. 4.9.

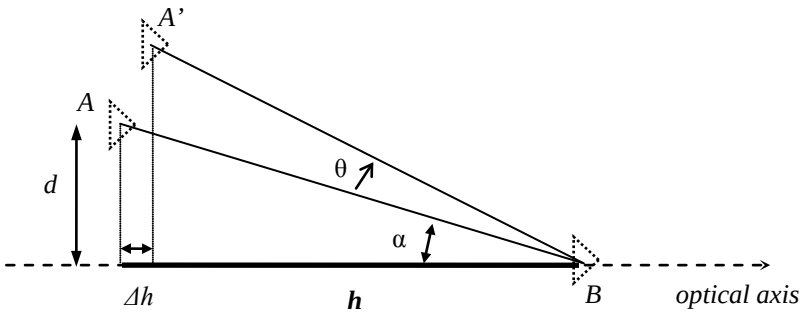

Fig. 4.9 Alignment error geometry

Consider points A and B representing two separate retroreflectors, and h is the OPD between two retroreflectors along optical axis, which is calibrated as part of the measurement reference. The angle between AB and the optical axis is α. If this angle changes by θ, the change in the OPD measured, approximated to second order in θ, is

$$\begin{aligned} \Delta h &= h(1-\cos\theta) + d\sin\theta \\ &\approx h\theta^2/2 + \theta d \end{aligned} \tag{4.7}$$

That is, for a small incoming laser direction variation, the OPD difference includes a first order term θd and a second order term $h\theta^2/2$. Since the separation between retroreflectors, d, is 10 mm, the first order rotation term is significant. The primary manifestation of this problem is that it increases sensitivity to alignment errors in the reference interferometer. As a result of alignment instability in interferometer, the incoming laser beam must be realigned periodically with the reference interferometer. If repeated alignments are carried out with an angle uncertainty θ, the effective length of the reference will change as indicated by Eq. (4.7).

Hence we propose a triplet retroreflector structure to reduce the sensitivity to the alignment error shown in Fig. 4.10, where A_1, A_2 and B represent three retroreflectors, A_1 and A_2 are equally distributed along y axis perpendicular to the optical axis or x axis. Thus, the distance d of A_1 to the optical axis is equal to that of A_2 to the axis.

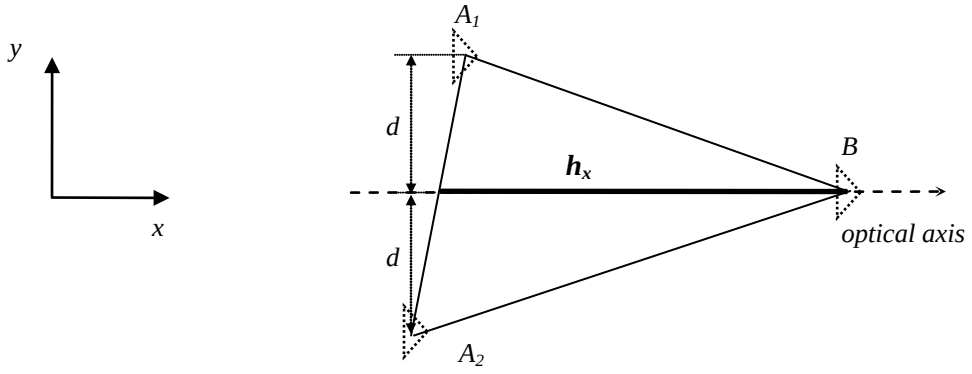

Fig. 4.10 Schematic of a first order rotation invariant module

And the OPD from point B to the midpoint of A_1 and A_2 is considered as the measurement reference or module distance h_x, given in Eq. (4.8).

$$h_x = B_x - (A_{1x} + A_{2x})/2 \tag{4.8}$$

where B_x, A_{1x}, A_{2x} are x coordinates of the three points. Assuming the coordinates of A_1, A_2, B are $\{x,d,1\}$, $\{-x,d,1\}$ and $\{h,0,1\}$ then $h_x = h$.

h_x is invariant to the first order rotation. That is, assuming an alignment uncertainty θ degrees exist, the first order term of the change in the OPD is removed from Eq. (4.7). This can be proved by mathematical calculation using the rotation matrix.

We then derive h_x before and after rotation. In this particular case, rotation occurs around point B. Without the loss of generality, a more general situation is that rotation around an arbitrary point (x_c, y_c), which can be expressed as translation from a point (x_c, y_c) to the origin (0, 0), rotation around the origin and translation from the origin to the point (x_c, y_c). In Eq. (4.9), R is a rotation matrix. T_1 is a translation from (x_c, y_c) to (0, 0). T_2 is a translation from (0, 0) to (x_c, y_c).

$$R = \begin{bmatrix} \cos\theta & -\sin\theta & 0 \\ \sin\theta & \cos\theta & 0 \\ 0 & 0 & 1 \end{bmatrix}; T_1 = \begin{bmatrix} 1 & 0 & -x_c \\ 0 & 1 & -y_c \\ 0 & 0 & 1 \end{bmatrix}; T_2 = \begin{bmatrix} 1 & 0 & x_c \\ 0 & 1 & y_c \\ 0 & 0 & 1 \end{bmatrix}; \tag{4.9}$$

The general form for a rotation about the point (x_c, y_c) is T_2RT_1 shown in Eq. (4.10).

$$T_2RT_1 = \begin{bmatrix} \cos\theta & -\sin\theta & x_c - x_c\cos\theta + y_c\sin\theta \\ \sin\theta & \cos\theta & y_c - y_c\cos\theta - x_c\sin\theta \\ 0 & 0 & 1 \end{bmatrix} \tag{4.10}$$

Applying this general rotation matrix around an arbitrary point (x_c, y_c), the new coordinates of A_1, A_2, B are computed as

$$
\begin{aligned}
T_2RT_1A_1 &= \{x\cos\theta + x_c - x_c\cos\theta - d\sin\theta + y_c\sin\theta,\ x\cos\theta + y_c + d\cos\theta - y_c\cos\theta - x_c\sin\theta, 1\} \\
T_2RT_1A_2 &= \{-x\cos\theta + x_c - x_c\cos\theta + d\sin\theta + y_c\sin\theta,\ -x\cos\theta + y_c - d\cos\theta - y_c\cos\theta - x_c\sin\theta, 1\} \\
T_2RT_1B &= \{x_c + h\cos\theta - x_c\cos\theta + y_c\sin\theta,\ y_c - y_c\cos\theta + h\sin\theta - x_c\sin\theta, 1\}
\end{aligned}
\tag{4.11}
$$

Thus the OPD from the point B to the midpoint of A_1 and A_2, h_x', after rotation, is expressed in Eq. (4.12).

$$
\begin{aligned}
&(T_2RT_1B - (T_2RT_1A_2 + T_2RT_1A_1)/2)\{1, 0, 0\} \\
&= x_c + h\cos\theta - x_c\cos\theta + y_c\sin\theta + (-2x_c + 2x_c\cos\theta - 2y_c\sin\theta)/2 \\
&= h\cos\theta
\end{aligned}
\tag{4.12}
$$

It is demonstrated that the difference before and after rotation is $h(1-\cos\theta) \approx h\theta^2/2$. Compared with Eq. (4.7), only the second order term remains. If we apply h_x as the measurement reference, the sensitivity to alignment errors can be greatly reduced. Actually this triplet module can be extended to a more general model. Considering three points A_1, A_2, and B as shown in Fig. 4.9 but not equally separated along y axis, instead, the ratio between distance from A_1 to B along y axis, d_1, and A_2 to B , d_2, is shown in Eq. (4.13).

$$
\frac{d_1}{d_2} = \frac{m}{n} \tag{4.13}
$$

Where, m and n are integer numbers. Then the general expression of this triplet module distance h_G can be expressed as

$$
h_G = B_x - \frac{nA_{1x} + mA_{2x}}{m + n} \tag{4.14}
$$

Note that since this triplet module contains three retroreflectors, employing 5 retroreflectors in this study means that multiple reference heights can be generated by the use of different triplet combinations of retroreflectors.

4.3.6 Summary

In many aspects the sources of error and uncertainty of the MHTIT system are similar to those of many interferometers, such as air refractive index variation due to environmental disturbance and mechanical vibration (Cabral & Rebordão, 2007). But unique aspects of MHTIT must also be taken into account. Multiple reference heights are used instead of only one reference height as in conventional wavelength scanning interferometers. The number, spacing and long-term reproducibility of multiple reference heights can impact measurement reliability and accuracy. By conducting a numerical simulation, a good reference height spacing design is proposed to compromise the phase unwrapping robustness and reference height uncertainty with the given system noise model. We observed OPDs variation due to thermal gradients in this system because of the long optical path, which impacts long-term stability of the multiple reference heights. Another important factor in reducing long-term stability of the reference heights is the alignment error. The alignment errors induced by the angular uncertainties were analyzed. And a rotation invariant triplet module was proposed to compensate for this error. We also investigated the error sources in the phase measurement method by applying spatial fringe analysis. The correct orientation of the retroreflector and employment of Gaussian window filter improved the phase measurement accuracy.

4.4 Conclusions

In this chapter, we presented the measurement performance of the multiple height-transfer interferometric technique (MHTIT) for discontinuous surface height

measurements. Gauge block measurements under the lab environment showed about a 0.3 µm uncertainty for a 50.8 mm step height at a confidence level of 95%. A measurement uncertainty analysis was conducted, demonstrating that a MHTIT measurement is analogous to a WSI measurement but has its own characteristics. The measurement accuracy of the MHTIT is also determined by uncertainties in the multiple reference heights and in the phase measurements, while the MHTIT requires an optimal selection of multiple reference height spacing to conciliate phase unwrapping robustness and measurement uncertainty. Other factors limiting the measurement performance, such as phase measurements using the spatial fringe analysis and alignment errors, were discussed and possible techniques for minimizing the errors were presented.

CHAPTER 5
APPLICATION TO THICKNESS MEASUREMENTS OF TRANSPARENT PLATES

5.1 Introduction

Metrology systems for measuring large optics with high precision are greatly needed in many applications. But it has been difficult to achieve thickness measurements of transparent plates by nondestructive interferometric methods. A common problem lies in the complex interference fringe patterns arising from multiple-surface reflections (Schwider, 1983). Standard phase-shifting interferometry (Greivenkamp, 1992) suffers from a fundamental limitation in that the algorithms assume pure two-beam interference.

In wavelength-scanning interferometry, the modulation frequency of the interference fringes depends on the optical path difference (OPD) between interference surfaces. Therefore, by careful control of the distances between the reflecting surfaces so that the frequencies do not overlap in Fourier domain, the necessary separation of individual OPDs by applying a Fourier transform can be achieved (Okada, 1990; Suematsu, 1991; Groot, 2000). However, since the Fourier frequency analysis is very sensitive to the linearity of frequency tuning, the measured frequencies are subject to

systematic errors caused by tuning nonlinearity. For absolute distance measurements of thick plates in which a large tuning range is often required, the measurement performance is more susceptible to tuning nonlinearities. There have been several methods proposed to deal with the nonlinear laser tuning (Glombitza, 1993; Iiyama, 1996; Waagaard, 2005; Moore, 2008). One way is to focus on the design and execution of a tunable laser source with a tuning curve that is linear in time (Wang, 1993; Huang, 1994; Tsuji, 1997). Depending on the laser source, this approach can be difficult and, in general, is less convenient than the other options. Rather than linearizing the laser sweep, a second technique uses an auxiliary interferometer to continuously monitor the phase variation of a fixed OPD reference cavity, and then synthetic wavelengths are measured at each sampling interval to apply a discrete Fourier transform (Deck, 2002, 2003). The use of the discrete Fourier transform avoids the requirement imposed by the fast Fourier transform algorithm that data be sampled at equal intervals of the independent variable, provided that the size of each unequal interval be known. But for the large aperture optical measuring system, the necessity of expensive high resolution, high speed camera limits its applications in industries.

In this chapter, we present a Fourier transform based wavelength-stepping interferometric method for the ShaPix measuring system to determine the thickness of 300 mm × 300 mm large aperture optics in one measurement without high speed camera. 2π phase ambiguity due to discrete wavelength stepping is resolved by applying the multiple height-transfer interferometric technique and the reference array designed in the previous chapter. Systematic errors caused by nonlinearities in the wavelength stepping are reduced with more accurate synthetic wavelengths determined by the

unwrapped phase change and the OPD of the longest reference height. The measurements of a step height standard etched on a 3-mm quartz block are conducted to demonstrate the principle.

5.2 Theory

5.2.1 Thickness Measurement by Discrete Fourier Transform

Consider a measurement setup for a thick transparent plate as illustrated in Fig. 5.1.

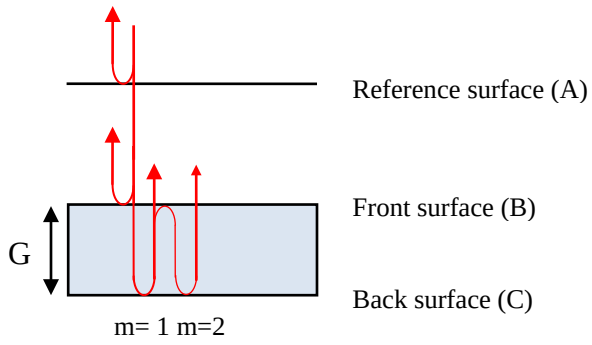

Fig. 5.1 A three-surface setup.

As shown in the figure, the combination of the reference, the front and the back surfaces of the setup produces 3 different 2-surface cavities (reference-front, reference-back, and front-back). Where, G is the physical thickness of a plate, the lines represent possible multiple reflections between surfaces, m=1 is for single reflection or 1st order reflection, m=2 is for double reflection or 2nd order reflection and so on. Denoting 3 surfaces as surface A, B and C, the electric fields on single reflection from each of the three surfaces can be represented respectively as

$$E_A = Ae^{i\phi_A},\ E_B = Be^{i\phi_B},\ E_C = Ce^{i\phi_C}, \tag{5.1}$$

The total electric field is given by

$$E_T = E_A + E_B + E_C \tag{5.2}$$

The interferogram produced by the interference from 3 surfaces can be expressed as

$$\begin{aligned} I_T &= E_T E_T^* \\ &= A^2 + B^2 + C^2 + 2AB\cos(\phi_A - \phi_B) + 2BC\cos(\phi_B - \phi_C) + 2AC\cos(\phi_A - \phi_C) \\ &= S + 2AB\cos(\Phi_{AB}) + 2BC\cos(\Phi_{BC}) + 2AC\cos(\Phi_{AC}) \end{aligned} \tag{5.3}$$

Where $S=A^2+B^2+C^2$, the subscripts Φ_{AB}, Φ_{BC}, and Φ_{AC} represent the phase difference between respective surfaces. Similarly, if electric fields from the double reflections and higher order reflections are also taken into account, the interferogram can be expressed at a pixel coordinate *(x, y)* by a linear superposition of the interferograms from the combinatorial collection of 3 surfaces as shown in Eq. (5.4)

$$I(x,y) = a_0 + a_1\cos[\Phi_1(x,y)] + \sum_{k=2,3,\ldots} a_k\cos[\Phi_k(x,y)] \tag{5.4}$$

Where, the each phase Φ_k represents to an individual phase difference that may result from single or multiple reflections between surfaces. For example, if Φ_1 is the phase difference due to the single reflection between the front and back surfaces, then

$$\Phi_1(x,y) = 2n(x,y)G(x,y)\frac{2\pi\nu}{c} + \Theta \tag{5.5}$$

where *G(x, y)* is the physical thickness of the plate, *v* is the optical frequency of the laser light, *n(x, y)* is the refractive index of the test object and Θ is the constant phase change upon reflection at the surfaces. Tuning the laser frequency *v* continuously produces a phase-shift rate of

$$\frac{\partial \Phi_1(x,y)}{\partial t} = \frac{4\pi n(x,y)G(x,y)}{c}\gamma_\nu[1+\eta(x,y)] \tag{5.6}$$

Where $\gamma_\nu = \frac{\partial \nu}{\partial t}$ is the optical frequency tuning rate and the term η accounts for the index chromatic dispersion shown as

$$\eta = \frac{\nu}{n}\frac{\partial n}{\partial \nu} \tag{5.7}$$

Chromatic dispersion must be taken into account in the thickness measurement as a large wavelength shift is applied. For quartz at 833.22 nm, η is approximately 0.9%. If a perfect linear frequency tuning rate γ_ν is known, the interferogram intensity varies at a frequency *f* equal to

$$f(x,y) = \frac{L(x,y)}{c}\frac{\partial \nu}{\partial t} \tag{5.8}$$

Where *L* is the total optical path length (OPL) obtained from Eq. (5.6)

$$L(x,y) = 2n(x,y)G(x,y)[1+\eta(x,y)] \tag{5.9}$$

Thus, for a linear optical frequency sweep, each cavity in a wavelength scanning interferometer produces a constant interference frequency that depends on the total OPL of the cavity. Cavities can be separated and extracted in the temporal Fourier domain as

long as each cavity has a unique OPL. This is the fundamental principle lying behind transparent plate measurements by wavelength-scanning interferometry.

The frequencies of the cavities are identified by their corresponding peaks in the measured spectrum by conducting a temporal Fourier transform of the interference time history *I(x, y, t)* as shown

$$A(x, y, f) = \int_{-\infty}^{\infty} I(x, y, t) w(t) \exp(-i2\pi f t) dt \tag{5.10}$$

where *I(x, y, t)* is the interference intensity variation at the position *(x, y)* acquired at time *t*, and *w(t)* is the Fourier window function chosen to bandwidth limit the signal.

As optical frequency tuning departs from linearity, the frequency peaks obtained from the spectrum are both shifted and distorted. Nonlinear tuning effects are a practical concern, so a fast wavelength meter is required to provide the actual frequency during tuning. Alternatively, a reference interferometer is incorporated that consists of a separate interferometer cavity of known, fixed first-order OPL and the phase variation of this cavity is measured simultaneously with the main interferometer cavity during the tune (Deck, 2002, 2003). Because both interferometers experience the same tuning rate, the ratio of the frequencies is

$$f = \frac{L}{L_R} f_R \tag{5.11}$$

Where, L, L_R are the total OPL of the test and reference interferometer cavities, respectively. Thus the reference interferometer provides an independent measurement of the wavelength change and can account for nonlinear tuning effects. Substituting Eq. (5.11) into Eq. (5.10), we can write

$$A'(x,y,L) = \int_{-\infty}^{\infty} I(x,y,t)w(t)\exp\left(-i2\pi\frac{L}{L_R}f_R t\right)dt \tag{5.12}$$

Note that the reference interferometer phase evolution

$$\phi_R = 2\pi f_R t \tag{5.13}$$

with a change of variables $t \rightarrow \phi_R$, the OPL transform is obtained as

$$A'(x,y,L) = \int_{-\infty}^{\infty} I(x,y,\phi_R)w(\phi_R)\exp\left(-i\phi_R\frac{L}{L_R}\right)d\phi_R \tag{5.14}$$

In practice, the discrete transform is applied converting from continuous time to discrete time signals.

$$A''(x,y,L) = \sum_{j=1}^{P} I_j(x,y)w_j \exp(-i\phi_{Rj}L/L_R)\Delta\phi_{Rj} \tag{5.15}$$

Where the index j runs over P samples $I_1 \ldots I_P$ at different wavelengths. Then the OPL spectrum can be generated with

$$F(L) = \left|A''(L)\right|^2 \tag{5.16}$$

Each peak in the spectrum is corresponding to the OPL of a particular cavity.

Following the principle of wavelength-scanning interferometry (WSI), the resolution in this OPL measurement is determined by the shortest synthetic wavelength Λ_{min}, which relates to the maximum tuning range $\Delta\lambda$ as

$$\Lambda_{\min} = \frac{\lambda^2}{\Delta\lambda} \tag{5.17}$$

Where, λ is the center wavelength. On the other hand, the range of measurements is limited by the longest synthetic wavelength Λ_{max} that is expressed as

$$\Lambda_{\max} = \frac{\lambda^2}{\delta\lambda} \tag{5.18}$$

Where, $\delta\lambda$ is the minimum wavelength interval determined by the applied laser source.

In conventional WSI, an additional fast detector or phase meter is employed to record the phase evolution ϕ_R during scanning, and phase unwrapping is straightforward since oversampling phase data assures that two neighboring phases are traceable and avoids the phase ambiguity problem. As discrete wavelength stepping is applied to replace continuous scanning and wrapped phase information is obtained at each wavelength, phase ambiguity may occur if the minimum wavelength step introduces a phase shift over 2π for the reference interferometer. These wrapped phases must be unwrapped with a phase unwrapping algorithm in order to compute the OPL transform.

In this study, multiple retroreflectors installed on a superinvar base in our setup act as the phase meters that are used in other wavelength-scanning interferometers. Their OPDs along the optical axis are used as the measurement references. Therefore, a two-step phase retrieval method for the reference interferometer in wavelength-stepping interferometry is proposed. First, a spatial fringe analysis technique is applied on the interference patterns generated on the retroreflector surfaces to measure the wrapped phase at each wavelength; second, we apply the multiple height-transfer interferometric technique (MHTIT) to unwrap the phase of the longest reference interferometer, which is then substituted in Eq. (5.16) to determine the overall OPL of the test object.

5.2.2 Fiducial Phase Extraction by Spatial Fringe Analysis

Spatial domain phase measurement methods have the advantage over time domain phase shifting methods in that only one interferogram is needed to extract the phase information while the latter requires multiple interferograms taken at different times (Takeda 1982). But it requires a specific period of the fringes and a smooth phase function for good accuracy (Massig, 2001; Vander, 2003). In this study, one single interferogram is captured at each wavelength so spatial domain methods are applied. To achieve a good measurement accuracy, a spatial carrier frequency was generated by tilting the array beam splitter, which allows controlled simultaneous generation of identically orientated fringes for all the retroreflector images as shown in Fig. 3.5.

Following the similar phase measurement procedure discussed in Chapter 3, we define the one way OPD of a tilted retroreflector with respect to the zero path position as

$$H(x,y) = x\sin(\alpha_x) + y\sin(\alpha_y) + H_o \tag{5.19}$$

Where α_x and α_y are tilting angles in x and y directions, H_o is the one way OPD at the coordinate center. The j^{th} wavelength interferogram at the camera detector array is proportional to the intensity

$$I_j(x,y) = I_O + I_R + 2\sqrt{I_O I_R}\cos\{\tfrac{4\pi}{\lambda_j}H(x,y)\} \tag{5.20}$$

Where, I_o, I_R are the intensities of reference and object beams, respectively, λ_j the free space wavelength of the light. No phase shift term exists in this equation.

After applying weighting function for sidelobe control and taking its Fourier transform (FT), the wrapped fringe phase at the coordinate center is obtained by

examining the complex phase of the FT at wavelength *j* where peak locates in the spectrum domain as Eq. (5.21) shows.

$$\phi_{Rj} = \mathrm{mod}(\frac{4\pi}{\lambda_j} H_0, 2\pi) \tag{5.21}$$

Since all the fringe area is used to calculate this phase, it is a high signal-to-noise ratio result that is not significantly influenced by poor quality single pixels. Hence, super-resolution of the peak position and phase is possible.

As discussed in the previous chapter, the orientation of the fringes is intentionally selected so that the side lobes induced by the cross hairs of the retroreflector do not contaminate the main peak by the interference fringes in the Fourier domain. Fig. 5.2 illustrates the measurement steps using the FT method. First, one 64×64 pixel area is extracted from the raw interferogram and padded with zeros, forming a 256×256 matrix; second, a Gaussian window function is applied for sidelobe control; third, a 2D FT on the area-of-interest is applied giving a Fourier spectrum and a phase map; finally, the wrapped phase of the center pixel of the retroreflector is obtained at the spectral position where its FT spectrum magnitude is maximum.

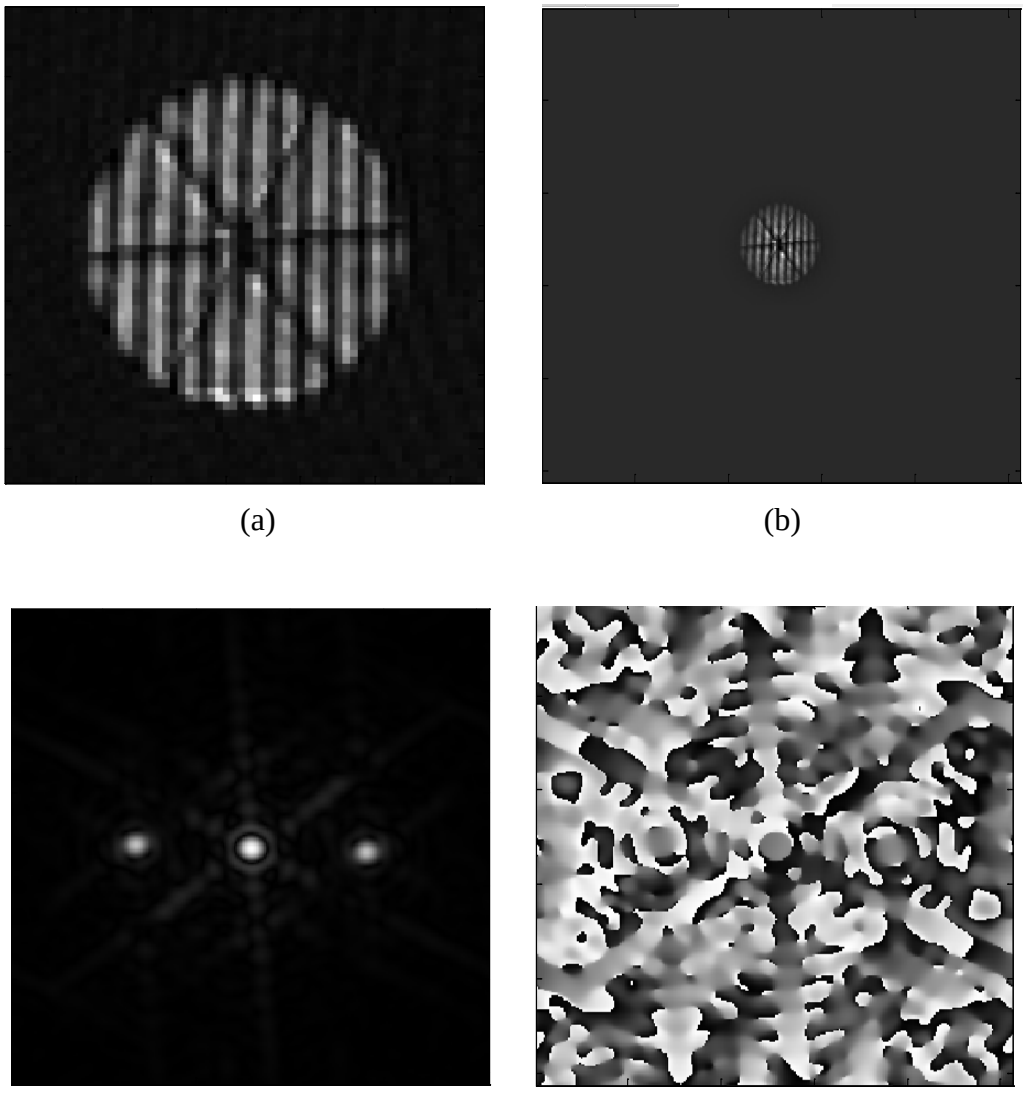

(a) (b)

(c) (d)

Fig. 5.2 (a) Extracted raw interferogram, (b) Gaussian filter with zero padding, (c) FT spectrum, (d) Phase map of FT

5.2.3 Phase Unwrapping by the MHTIT

Once the wrapped fringe phases are obtained at different wavelengths, a phase unwrapping algorithm is often needed to provide unwrapped phase information.

When two neighboring wavelengths are applied to the reference interferometer, the phase difference can be expressed by the well-known synthetic wavelength equation.

$$\Delta\Phi = 4\pi L_{ref}\left(\frac{1}{\lambda_n} - \frac{1}{\lambda_{n+1}}\right) \approx 4\pi L_{ref}\frac{\Delta\lambda}{\lambda^2} = \frac{4\pi L_{ref}}{\Lambda_n} \tag{5.22}$$

Where, λ_n, λ_{n+1} are two applied neighboring wavelengths; λ corresponds to the center wavelength; $\Delta\lambda = \lambda_{n+1} - \lambda_n$ is the wavelength interval between the two wavelengths; L_{ref} is the one-way OPD of the reference interferometer, and Λ_n is the synthetic wavelength that is approximated by $\lambda^2/\Delta\lambda$.

As shown in the equation, in order to avoid the phase ambiguity problem, i.e., when the phase difference between two neighboring wavelength steps is smaller than 2π, the multiplication of L_{ref} and $\Delta\lambda$ must be smaller than certain value. For example, if a 50 mm L_{ref} is applied in the measurement, the wavelength interval must be less than 6.4 pm (at 800 nm center wavelength). In practice, the wavelength step is determined by the tuning mechanism of the laser source, which in our case has a nominal minimum step of 20 pm. Thus, phase unwrapping is required to keep track of the phase shifts between different wavelengths.

We then applied the MHTIT to unwrap the phase shifts for the reference interferometer. The MHTIT takes the advantages of multiple reference heights that have different sensitivities to phase shifts. Small heights are used to remove phase ambiguity for large heights when wide wavelength intervals are applied. And the longest height is employed as the measurement reference, which provides the best measurement accuracy.

In this study, four different reference OPDs are applied for the phase unwrapping and we choose the proper shortest reference OPD L_1 so that the wavelength uncertainty does not cause fringe order ambiguity. Consequently, the fringe order difference q_{n1} can be determined correctly and thus the phase difference for the shortest reference OPD can be unwrapped as shown in Eq. (5.23).

$$\frac{\Lambda_n}{4\pi} = \frac{L_1}{2\pi q_{n1} + \Delta\phi_{n1}} = \frac{L_2}{2\pi q_{n2} + \Delta\phi_{n2}} = \frac{L_3}{2\pi q_{n3} + \Delta\phi_{n3}} = \frac{L_4}{2\pi q_{n4} + \Delta\phi_{n4}} \tag{5.23}$$

Theoretically, all four reference OPDs follow the same synthetic wavelength equation. The unwrapped phase $2\pi q_{n1} + \Delta\phi_{n1}$ obtained in the first step is then used to unwrap the phase difference for the next OPD. The resultant synthetic wavelength Λ_n, determined by the ratio between the reference OPD and phase difference, is then corrected to a new value with smaller uncertainty than that at the previous step. This iterative process terminates when all phase differences are unwrapped. The longest reference OPD L_4 provides the most accurate synthetic wavelength, which will be substituted into the OPL transform equation to calculate the thickness of the optical plates.

5.3 Experiments and Results

The measurement of a known step height etched on a transparent plate is presented to verify the principle of the proposed method. The ShaPix system consists of a pseudo-Fizeau interferometer equipped with a widely tunable laser and a reference array for measuring synthetic wavelengths. With a CCD detector of 2048×2048 pixels,

the system can directly measure the shape of 300 mm × 300 mm surfaces with a 150 μm lateral resolution, which provides an appropriate field of view for large aperture optics. This system is used in this study to measure the thickness of transparent plates.

The test object is a Wyko step height standard shown in Fig. 5.3, which consists of a 25 mm × 25 mm × 3 mm quartz block with a precisely etched uniform bar. The step height etched in quartz is calibrated by the manufacturer to be 10.06 ± 0.03 μm (traceable through NIST calibrated specimens). Thus, by comparing the thickness difference of the step height, the measurement capability of the proposed method can be demonstrated.

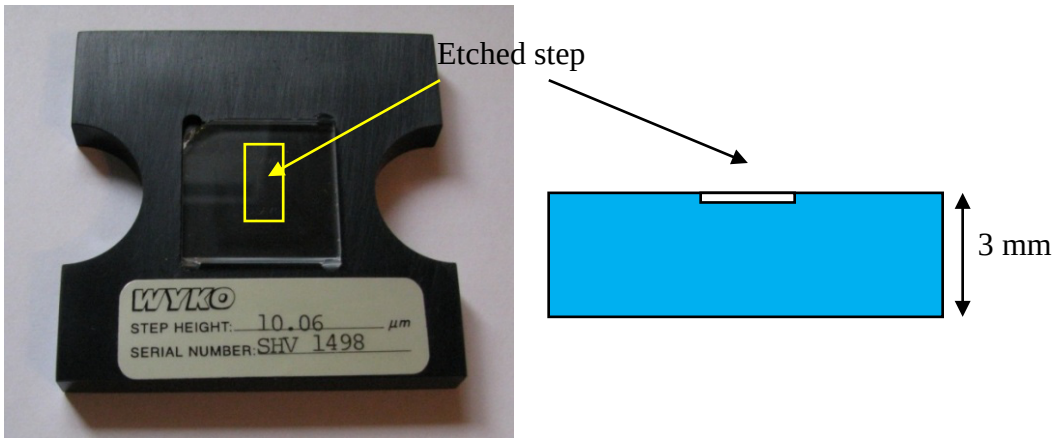

(a) (b)

Fig. 5.3 A 10-μm step height is etched in a quartz block: (a) Whole view of the test object, (b) Side view diagram

The experimental setup of the ShaPix measuring system is shown in Fig. 5.4. Compared to conventional Fizeau interferometers, this system splits the reference beam and the object beam by a variable beam splitter and inserts the light into polarization maintaining fibers, which avoids the use of a reference optical plate providing more flexibility for the reference beam. The reference fiber has extra length to compensate for

the free space propagation length of the object wave such that the zero path length difference is slightly above the object surface. Thus, we can easily configure the interferometer cavity such that each cavity of interest has a unique OPL.

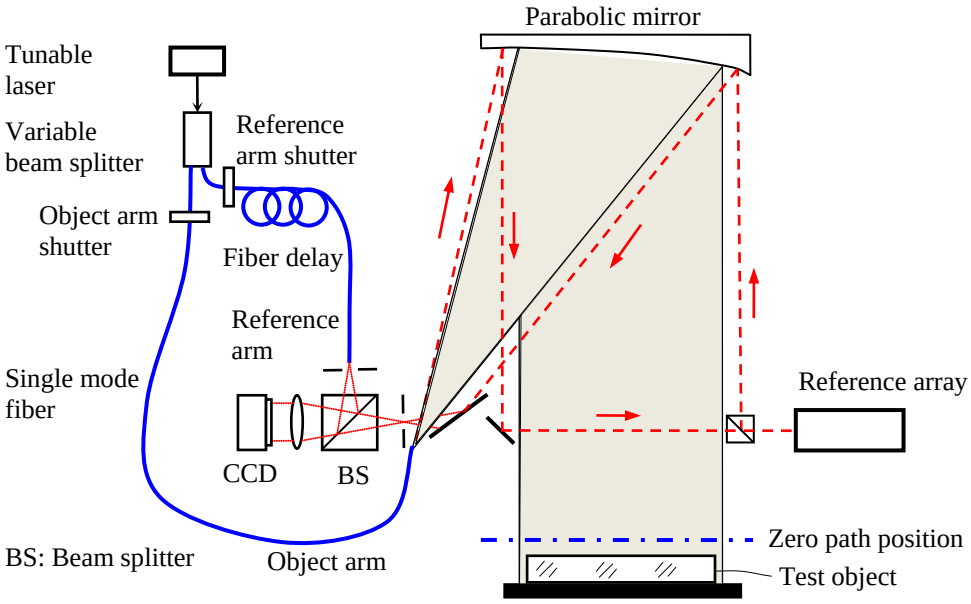

Fig. 5.4 Layout of the ShaPix system for testing a transparent plate

By closing the shutter on the reference arm, Fig. 5.5 (a) shows an observed raw interference fringes formed from reflections only between the front and back surfaces of the test plate. The high contrast fringes represent the variation in the optical thickness. Fig. 5.5 (b) shows the interferogram with multiple surface reflections. For a nominal optical thickness of 3-mm and a nominal refractive index of 1.45276 at 833 nm, the necessary scanning width $\Delta\lambda$ for a 2π phase shift is $\frac{\lambda^2}{2nd} \approx 0.08$ nm. We stepped the source wavelength linearly from 833.32 nm to 849.61 nm over a 16 nm bandwidth. 815 interference images were captured with an equal wavelength step of 0.02 nm. That is,

about 4 samples are captured for each phase period, thus satisfying the Nyquist sampling theorem requirement of at least 2 samples per phase period.

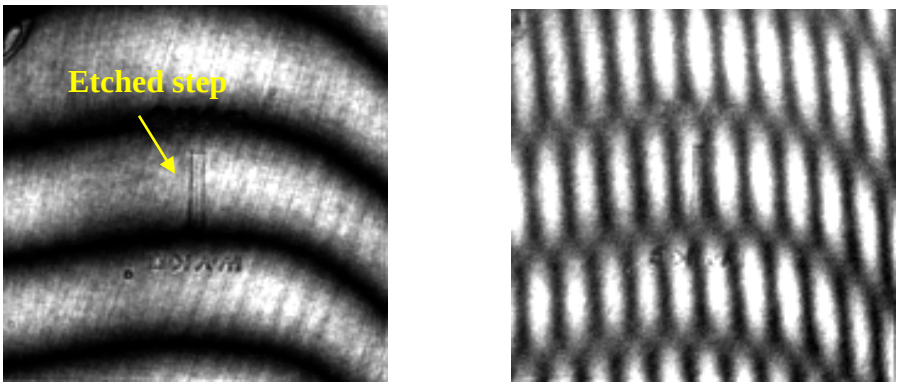

(a) (b)

Fig. 5.5 (a) Two-surface interferogram from front and back surfaces, (b) Interferogram with multiple surface reflections

For the two-step phase retrieval method, the spatial fringe analysis method was first applied to extract the wrapped phase information of each retroreflector following the same measurement steps explained in Section 3.3.2. Subtracting the corresponding phases of the center pixel of the retroreflector, the phase differences between retroreflectors were obtained. Then the MHTIT technique was employed to unwrap the phase difference for the longest reference height, which will be substituted in Eq. (5.16) to compute the overall OPL of the test object between the front and back surfaces. The four independent reference OPDs calibrated and employed in ascending order are 0.5 mm, 2.3 mm, 11.1 mm, 49.9 mm. Fig. 5.6 (a) represents wrapped phase variation of the shortest reference height over 16 nm wavelength shift; Fig. 5.6 (b) compares the unwrapped phase shift for both the shortest reference and the longest reference height, showing successful phase unwrapping by the MHTIT.

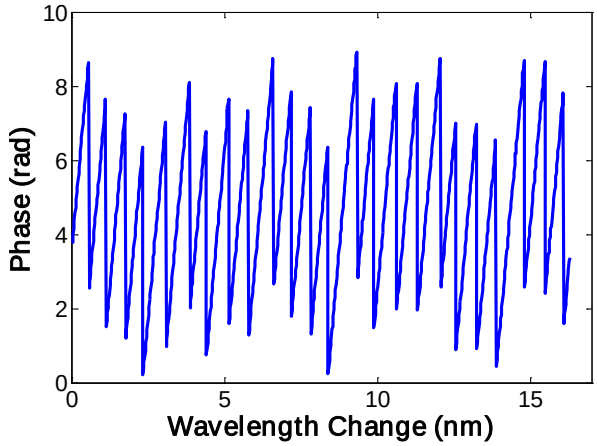

(a)

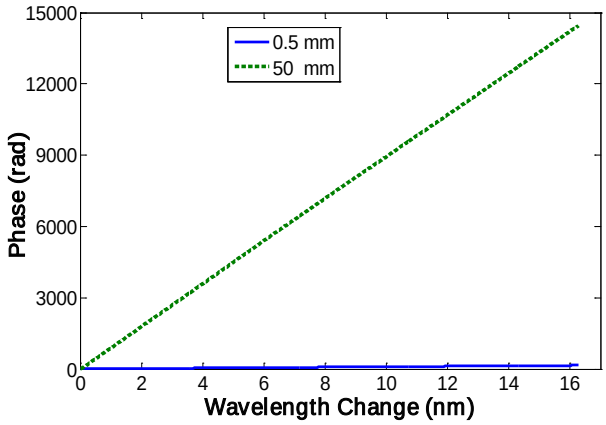

(b)

Fig. 5.6 (a) Wrapped phase variation of 0.5 mm height over a 16 nm width, (b) Unwrapped phase shift for 0.5 mm and 50 mm over a 16 nm width

With the phase shifts provided by the MHTIT and the known fixed-OPD reference interferometer, the synthetic wavelengths can be measured. We computed the synthetic wavelength in three different ways comparing the measurement performance of the MHTIT algorithm. The first and last wavelengths that have commanded values of 833.22 nm and 849.62 nm from the laser controller lead to calculating the commanded synthetic wavelength. Then the synthetic wavelength was measured by a Burleigh wavelength meter WA-1500 and the MHTIT. The air refractive index is 1.000271374 at

20°C, 101.325 KPa, and 50% relative humidity based on a modified version of the Edlén Equation (Birch & Downs, 1994). The results are shown in Table 5.1.

Table 5.1 Synthetic Wavelength from Commanded Output, Wavemeter Measurement and MHTIT Calculation

	Commanded wavelength (nm)	MHTIT calculation (nm)	Wavemeter measurements (nm)
λ_1 (in vacuum)	833.22		833.4475
λ_{end} (in vacuum)	849.62		849.7282
$\mathbf{\Lambda}$ (in air)	43424.13	43486.85	43487.79
$\boldsymbol{\varepsilon}_{\Lambda}$ (in air)	63.66	0.86	

The wavelength meter, with a relative measurement uncertainty of 2×10^{-7}, provides two wavelength values of 833.4475 nm and 849.7282 nm in vacuum, taken to be the measurement standard. Comparing two synthetic wavelengths computed from the commanded wavelength and from the MHTIT algorithm, it is shown that the synthetic wavelength error is reduced from 63.66 nm to 0.86 nm, indicating that the MHTIT reduces the wavelength tuning nonlinearity by measuring the synthetic wavelength more accurately.

Finally, the overall OPL of the test plate was calculated by finding the peak in the OPL spectrum. We used the Hanning window function for sidelobe control defined by

$$w(j) = (2/815)\cos^2 \pi(j-408)/815 \tag{5.24}$$

The profile of Hann window used in this study is shown in Fig. 5.7.

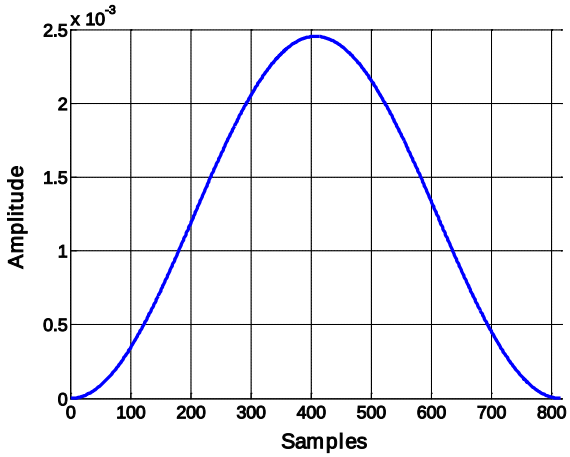

Fig. 5.7 Hanning window function applied in the measurement

A typical OPL transform spectrum over 10 mm range is shown in Fig. 5.8. The peak location indicates the measured first order OPL of the cavity at one pixel. The amplitudes of other higher order OPLs are much smaller than that of first order OPL due to reduced intensities resulting from multiple reflections. Note that thickness measurement is not sensitive to mechanical vibrations because movements due to the vibration have the same effect on both front and back surfaces and will be canceled out.

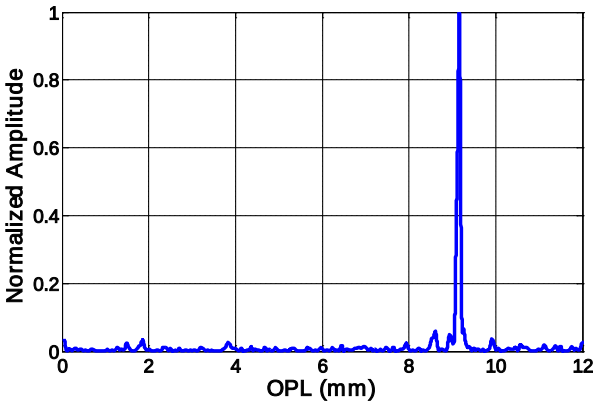

Fig. 5.8 An OPL transform spectrum at one pixel

During the measurement period, the temperature was regulated within 20±0.3^{o}C. Using the known coefficient of thermal expansion for quartz of 5.5e-7/ ^{o}C, the thickness

variation for the 10 μm step height is less than 1 nm. Eight measurements were conducted to measure the OPLs of all pixels. A typical two-dimensional OPL measurement result is shown in Fig. 5.9.

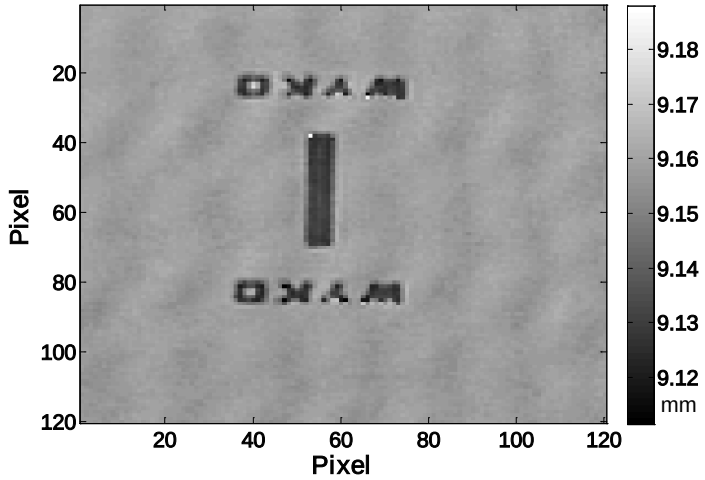

Fig. 5.9 A 2D OPL measurement display in grayscale

The general form of the measurement result agrees with the test surface, but a 3-μm ripple presents in the measurement result, which is induced by imperfect second-surface reflection suppression and can be alleviated by taking more samples during the wavelength tuning (Deck, 2003). The thickness of the step height is then calculated by comparing the averaged OPLs of the two surfaces for the etched area and clear area. Table 5.2 presents the experimental results of 8 measurements.

Table 5.2 Experimental Results

Measurement No.	Averaged OPL between top surface and back surface (mm)	Averaged OPL between etched surface and back surface (mm)	Thickness of the 10-μm step height (μm)
1	9.1600	9.1314	9.7
2	9.1585	9.1317	9.1
3	9.1586	9.1292	10.0

4	9.1584	9.1288	10.1
5	9.1578	9.1303	9.4
6	9.1586	9.1276	10.5
7	9.1594	9.1284	10.5
8	9.1587	9.1296	9.9
AVG±STD*	9.1587 mm±0.6 μm	9.1296 mm±1.3 μm	9.9 μm±0.5 μm

*AVG is the averaged value over 8 measurements, STD is the standard deviation.

The averaged OPL for 8 measurements is 9.1587 mm with a standard deviation of 0.6 μm between the top and back surfaces of the block, while that of the etched step surface is 9.1296 mm. Note that the OPL difference (ΔOPL) includes a round-trip optical path in the quartz material, so the thickness of the step height based on Eq. (5.9) is obtained as

$$G = \frac{\Delta OPL}{2n(1+\eta)} \tag{5.22}$$

Where $n = \frac{n_{quartz}}{n_{air}} \approx n_{quartz}$. With the known index of 1.45276 and η approximately 0.9% at 833.32 nm wavelength for quartz, the measured thickness of the step height is 9.9 μm with the standard deviation of 0.5 μm, which agrees with the specification of the step height standard.

5.4 Summary and Conclusions

We have proposed a thickness measurement method for thick transparent plates using a wavelength-stepping pseudo Fizeau interferometer and a discrete Fourier transform. Thickness between the top and bottom surfaces of the test object was measured by wavelength-stepping interferometry in which the wavelength was stepped

from 833 nm to 849 nm. Systematic errors caused by nonlinearities in the wavelength stepping of the laser were reduced by a multiple reference array and a multiple height transfer interferometric technique. A 25 mm × 25 mm × 3 mm quartz block with a precisely etched step height was measured to sub-micron thickness accuracy. The development of a wavelength stepping and phase unwrapping algorithm avoided the requirement for a high speed camera with many pixels, making it more suitable for high definition, large aperture optics measurements.

CHAPTER 6
CONCLUSIONS, CONTRIBUTIONS AND FUTURE WORK

6.1 Conclusions

This doctoral research is focused on developing effective and efficient interferometric measuring methods to increase the absolute distance measurement capabilities of a holographic metrology system. The effectiveness of the approach is demonstrated by achieving large area surface absolute distance measurements of industrial parts using a proposed calibration artifact installed in the system. The uncertainty analysis of the method is conducted by measuring a known-height gauge-block in the lab environment. Primary error sources related to the measurements are discussed and possible methods are proposed to further improve the measurement performance. We have also applied this method to measure the thickness of thick transparent plates which is of significance in many applications.

First, a multiple height-transfer interferometric technique (MHTIT) is developed based on the concepts of multiple-wavelength interferometry (MWI) and wavelength-scanning interferometry (WSI). It records interferograms at several discrete wavelengths in the same way as MWI does, and employs reference interferometers analogous to WSI to avoid the wavelength accuracy requirement. A low cost calibration

subsystem is proposed using multiple retroreflectors mounted on a superinvar base. By applying the MHTIT and multiple accurately calibrated reference heights, full surface absolute distance measurements of industrial parts such as valve body and pump housing are successfully conducted, demonstrating the applicability of the method in industrial applications.

Second, the measurement uncertainty of the technique is analyzed as determined by the uncertainties in the reference height, the reference phase and the object phase. Repeated known-height gauge block measurements are performed in the lab environment, presenting a measurement uncertainty of 6.2 ppm at a confidence level of 95%. To achieve better performance of a MHTIT measurement, such as more robustness of the phase unwrapping algorithm and better measurement accuracy, primary error sources are investigated. Possible techniques to minimized errors are proposed.

Finally, we apply this method to another important measurement application: thickness measurements of thick transparent plates. Conventional phase shifting interferometry has difficulty in achieving the measurements due to the complex interference fringes from the multiple surface reflections. WSI can measure the absolute thickness of transparent plates by differentiating OPDs in the Fourier domain. However, for the large aperture optical measuring system, the necessity of expensive high resolution, high speed camera limits its applications in industries. We present a Fourier transform based wavelength-stepping interferometric method for the Coherix metrology system that can be used to determine the thickness of 300 mm × 300 mm large aperture optics in one measurement without a high speed camera. The measurements of a step

height standard etched on a 3-mm quartz block are conducted to demonstrate the principle with sub-micron accuracy.

6.2 Contributions

The main contributions of this dissertation are summarized as follows:

- A multiple height-transfer interferometric technique has been developed based on concepts from both multiple wavelength interferometry and wavelength scanning interferometry (Yu, Aleksoff, & Ni, 2011). By making use of multiple accurately calibrated reference heights, this technique provides a way to unwrap the synthetic phases induced by multiple wavelengths of the tunable laser source, and to determine the synthetic wavelengths by the ratio of reference height and corresponding synthetic phases. A modified Fourier transform peak finding algorithm is proposed to provide object phase unwrapping. Thus it relaxes the requirement of knowing accurate wavelength information for MWI while maintaining its advantages. This new technique reduces the sensitivity to certain types of noise, allowing it to be more suitable for large area surface measurements with large height difference in industrial environments. This improved extension for MWI can benefit precision manufacturing by improving product quality and reducing warranty cost.

- We present a theoretical uncertainty analysis for the MHTIT, which is proved to have the same uncertainty equation as WSI (Yu, Aleksoff, & Ni, Accuracy of a multiple height-transfer interferometric technique for absolute distance

metrology). The measurement accuracy of the MHTIT is examined by performing repeated known-height gauge block measurements. Primary measurement error sources that are characteristic of the proposed technique are discussed. The number, spacing and long-term reproducibility of multiple reference heights can impact measurement reliability and accuracy. By conducting a numerical simulation, a good reference height spacing design is proposed to compromise the phase unwrapping robustness and measurement uncertainty with the given system noise model. Reference optical path difference variation due to thermal gradients in the measuring system is analyzed to study its impact to the long-term repeatability and reproducibility of the measurements. And a rotation invariant module is proposed to compensate for the alignment error induced by the angular uncertainty of the reference array. We also investigate the error sources in the phase measurement method by applying spatial fringe analysis. The correct orientation of retroreflector, interferometric fringes and employment of the Gaussian window filter improve the phase measurement accuracy.

- A wavelength-stepping interferometry combined with the MHTIT is proposed for transparent plate thickness measurements (Yu, Aleksoff, & Ni, Thickness measurement of transparent plates by wavelength stepping interferometry and a multiple height-transfer interferometric technique). Wavelength stepping allows practical high-resolution and large aperture measurements. Systematic errors caused by nonlinearities in laser source stepping are reduced with synthetic wavelengths measured by the reference array using the MHTIT.

6.3 Future Work

Interferometric absolute distance metrology based on the concept of synthetic wavelengths is one of the most interesting techniques for dimensional metrology. Synthetic wavelengths can be generated from utilizing two or more discrete wavelengths (MWI), or via a wavelength sweep (WSI). The MHTIT provides a complementary way to combine the advantages of both techniques by offering a unique phase unwrapping algorithm to achieve reliable measurements on industrial parts. The combinations of those advantages can be further extended to other research areas. A number of future research topics are suggested following the studies in this dissertation:

- WSI can measure thickness of transparent plates by differentiating optical path differences from multiple surface interferences in the Fourier domain. But it requires a large tuning range to achieve good accuracy for thick plates, which needs a lot of samples to suppress the multiple reflection interference intensity noises. Imperfect second-surface reflection suppression induces the undesirable ripple pattern on the measurement results shown in Fig. 5.9, decreasing the measurement accuracy. To improve the measurement accuracy of the transparent plate thickness measurement, it is possible to combine WSI and MWI in a different way. Instead of stepping over a large tunable range with equal wavelength interval to apply OPL transform for thickness measurements, a two-step thickness measurement scheme similar to traditional MWI can be proposed. First, by scanning the wavelength over a short wavelength interval $\delta\lambda$ and applying the WSI algorithm with enough samples, accurate phase information corresponding to the OPL of thickness can be extracted based on the

frequency analysis at the specific wavelength (Deck, 2003). Then the FT peak finding algorithm is applied with accurately known multiple wavelengths (measured by wavelength meters or the MHTIT) over a large wavelength bandwidth $\Delta\lambda$ ($>>\delta\lambda$) to achieve the thickness measurements. This measurement process relies on the phase information at multiple wavelengths instead of pure intensity information, thus could reduce the number of samples needed, and make it less sensitive to environmental noises leading to accurate results.

- The concept of applying multiple frequencies for phase unwrapping has been introduced to other optical measurement methods such as fringe projection techniques as “temporal phase unwrapping”. By varying the spatial frequencies (corresponding to the fringe densities) of the projected fringe patterns, discontinuous surface profile can be determined by unwrapping the phase at each pixel over time (Saldner & Huntley, 1997). But it requires an iterative calculation procedure and phase differences between successive images are within the range $-\pi$ to π. In this study, MWI applies a Fourier domain peak finding algorithm that takes all different wavelengths/frequencies into account simultaneously, which avoids the necessity of phase unwrapping. Hence, an application of the MWI peak finding algorithm to fringe projection techniques would be of interest to reduce the number of projected fringe patterns with different spatial frequencies, which can facilitate the measurement process and have potentials for manufacturing inline applications.

- MWI allows phase unwrapping for each pixel independently, and hence the process can be applied to rough, curved, and discontinuous surfaces. The basic

question addressed is what distribution of wavelengths should be used to optimize the height measurement performance. The height measurement characteristics of MWI can be characterized by a Power Height Response Function (PHRF), as expressed by Eq. (2.3). It is desirable to design a PHRF with low side lobes levels (in order to avoid mistakenly picking a sidelobe for the mainlobe and thus giving a wrong result), a narrow main lobe (in order to get better height resolution), low sensitivity to errors and noise in the system (in order to have robustness to laser frequency errors, object vibration, air turbulence, photon noise and detector noise, and surface roughness). At the same time we want to minimize the total number of frequencies in order to speed the data acquisition time and maximize the ambiguity-free-range, i.e., to have a larger range of heights that can be measured unambiguously. These goals are not compatible, and hence tradeoffs need to be made depending on what is the most important for the particular system. Therefore, an optimal selection criterion for the number and distribution of multiple wavelengths could be valuable in practice.

APPENDIX

Least-Squares Method of Phase-Shifting Analysis

The LSM of phase-shifting analysis has been described by several authors (Bruning, et al., 1974; Greivenkamp J., 1984; Greivenkamp & Bruning, 1992). Because it is suitable for use in conjunction with Fourier transform global phase step measurement algorithm, a brief outline of the method is presented here. The LSM allows the reconstruction of wave-front data in phase-shifting interferometry when arbitrary global phase-shifting steps are known. The N phase steps are defined as a set of N real values $\{\Delta_n\}$. For a fixed point on the measurement plane, we write the intensity as

$$\begin{aligned} I_n &= A + B\cos[\phi + \Delta_n] \\ &= a_0 + a_1\cos\Delta_n + a_2\sin\Delta_n \end{aligned} \tag{A1}$$

Here the phase steps Δ_n were separate from the unknown phase ϕ by definitions

$$\begin{aligned} a_0 &\equiv A, \\ a_1 &\equiv B\cos\phi, \\ a_2 &\equiv -B\sin\phi, \end{aligned} \tag{A2}$$

These are three unknowns for which we must solve. Because the phase steps are known as a priori, the $sin\Delta_n$ and $cos\Delta_n$ terms are simply the scalar coefficients of the unknown a_1, a_2 and are identical for all points in the measurement domain.

When we apply the method of least squares at each point, the goal is to minimize the error function E^2, defined as

$$E^2 \equiv \sum_{n=1}^{N}[I_n - a_0 - a_1 \cos\Delta_n - a_2 \sin\Delta_n]^2 \tag{A3}$$

The error function is related to the fit variance, where it is assumed that each measurement point contains the same uncertainty.

We minimize E^2 by differentiating Eq.(A3) with respect to the three unknown a_0, a_1, a_2. The resultant expression can be written in matrix form:

$$\begin{bmatrix} N & \sum\cos\Delta_n & \sum\sin\Delta_n \\ \sum\cos\Delta_n & \sum\cos^2\Delta_n & \sum\cos\Delta_n\sin\Delta_n \\ \sum\sin\Delta_n & \sum\cos\Delta_n\sin\Delta_n & \sum\sin^2\Delta_n \end{bmatrix} \times \begin{bmatrix} a_0 \\ a_1 \\ a_2 \end{bmatrix} = \begin{bmatrix} \sum I_n \\ \sum I_n\cos\Delta_n \\ \sum I_n\sin\Delta_n \end{bmatrix} \tag{A4a}$$

$$\boldsymbol{A}\boldsymbol{a} = \boldsymbol{b} \tag{A4b}$$

Here $\sum$ is a shorthand notation representing the sum over the N measurements, with n as the summation index. The symmetric matrix $\boldsymbol{A}$, call the curvature matrix, depends only on the known phase shifts, whereas the vector $\boldsymbol{b}$ contains the measured interferogram data. The solution for the coefficient vector $\boldsymbol{a}$ requires inverting $\boldsymbol{A}$ and premultiplying both sides of Eq. (A4b):

$$\boldsymbol{a} = \boldsymbol{A}^{-1}\boldsymbol{b} \tag{A5}$$

When there are three or more unique phase steps, the rows will be independent and $\boldsymbol{A}$ will be invertible. Once $\boldsymbol{a}$ is known, the phase ϕ is easily found as

$$\phi = \tan^{-1}\left[\frac{-a_2}{a_1}\right] \tag{A6}$$

BIBLIOGRAPHY

Aleksoff, C. C. (2010). Discrete step wavemeter. *7790*, p. 77900H. Proceedings of the SPIE.

Aleksoff, C. (2006). Multi-wavelength digital holographic metrology. *6311*, pp. 63111D-1-7. Proceedings of the SPIE.

Barwood, G. P., Gill, P., & Rowley, W. R. (1998). High-accuracy length metrology using multiple-stage swept-frequency interferometry with laser diodes. *Measurement Science Technology , 9*, 1036-1041.

Bechstein, K. H. (1998). Absolute interferometric distance measurements applying a variable synthetic wavelength. *Journal of Optics , 29*, 179-182.

Beheim, G., & Fritsch, F. (1985). Remote displacement measurements using a laser diode. *Electronics Letters , 21*, 93-94.

Birch, K. P., & Downs, M. J. (1994). Correction to the updated Edlen equation for the refractive index of air. *Metrologia , 31*, 315–316.

Bitou, Y., & Seta, K. (2000). Gauge Block Measurement Using a Wavelength Scanning Interferometer. *Japanese Journal of Applied Physics , 39*, 6084-6088.

Boef, A. J. (1987). Interferometric laser range finder using a frequency modulated diode laser. *Applied Optics , 26*, 4545-4550.

Born, M., & Wolf, E. (1999). *Principles of Optics* (7th ed.). Cambridge University Press.

Bourdet, G. L., & Orszag, A. G. (1979). Absolute distance measurements by CO2 laser multiwavelength interferometry. *Applied Optics , 18*, 225-227.

Bruning, J., Herriott, D., Gallagher, J., Rosenfeld, D., White, A., & Brangaccio, D. (1974). Digital wavefront measuring interferometer for testing optical surfaces and lenses. *Applied Optics , 13*, 2693-2703.

Cabral, A., & Rebordão, J. (2007). Accuracy of frequency-sweeping interferometry for absolute distance metrology. *Optical Engineering , 46*, 073602.

Carrara, W. G., Goodman, R. S., & Majewski, R. M. (1995). *Spotlight Synthetic Aperture Radar.* Boston: Artech House.

Chen, M., Guo, H., & Wei, C. (2000). Algorithm immune to tilt phase-shifting error for phase-shifting interferometers. *Applied Optics , 39*, 3894-3898.

Cheng, Y. Y., & Wyant, J. C. (1984). Two-wavelength phase shifting interferometry. *Applied Optics , 23*, 4539-4543.

Creath, K. (1988). Phase-measurement interferometry techniques. *Progress in Optics , 26*, 351-393.

Creath, K. (1987). Step height measurement using two-wavelength phase-shifting interferometry. *Applied Optics , 26*, 2810–2816.

Dändliker, R. (1992). Distance measurements with multiple wavelength techniques. *2nd Internat. Workshop on High Precision Navigation*, (pp. 159-170).

Dändliker, R., Hug, K., Politch, J., & Zimmermann, E. (1995). High-accuracy distance measurements by multiple-wavelength interferometry. *Optical Engineering , 34*, 2407-2412.

Dändliker, R., Thalmann, R., & Prongué, D. (1988). Two-wavelength laser interferometry using superheterodyne detection. *Optics Letter , 13*, 339-341.

Deck, L. L. (2002). Absolute distance measurements using FTPSI with a widely tunable IR laser. *Interferometry XI: Applications. 4478*, pp. 218–226. Proceedings of SPIE.

Deck, L. L. (2003). Fourier-Transform Phase-Shifting Interferometry. *Applied Optics , 42*, 2354-2365.

Dobroiu, A., Lagofatu, P. C., Apostol, D., & Damian, V. (1997). Statistical self-calibrating algorithm for three-sample phase-shift interferometry. *Measurement Science and Technology , 8*, 738-745.

Falaggis, K., Towers, D. P., & Towers, C. E. (2009). Multiwavelength interferometry: extended range metrology. *Optics Letters , 34*, 950-952.

Fercher, A. F., Hu, H. Z., & Vry, U. (1985). Rough surface interferometry with a two wavelength heterodyne speckle interferometer. *Applied Optics , 24*, 2181-2188.

Fercher, A. F., Hu, H. Z., & Vry, U. (1985). Rough surface interferometry with a two-wavelength heterodyne speckle interferometer. *Applied Optics , 24*, 2181-2188.

Fraser, C. S. (1992). Photogrammetric Measurement to One Part in a Million. *Photogrammetric Engineering and Remote Sensing , 58*, 305-310.

Gåsvik, K. J. (2002). *Optical metrology* (3rd ed.). West Sussex, Eng.: J. Wiley & Sons.

Gillard, C. W., & Buholz, N. E. (1982). Progress in absolute distance interferometry. *Proceedings of SPIE*, (pp. 368-376).

Glombitza, U., & Brinkmeyer, E. (1993). Coherent frequency-domain reflectometry for characterization of single-mode integrated-optical waveguides. *Journal of Lightwave Technology , 11*, 1377-1384.

Goldberg, K. A., & Bokor, J. (2001). Fourier-transform method of phase-shift determination. *Applied Optics , 40*, 2886-2894.

Goodwin, E. P., & Wyant, J. C. (2006). *Field Guide to Interferometric Optical Testing.*

Greivenkamp, J. E., & Bruning, J. H. (1992). *Phase shifting interferometry* (2nd ed.). New York: Wiley.

Greivenkamp, J. (1984). Generalized data reduction for heterodyne interferometry. *Optical Engineering , 23*, 350-352.

Groot, P. d. (1991). Interferometric laser profilometer for rough surfaces. *Optics Letters , 16*, 357-359.

Groot, P. J. (1995). Derivation of algorithms for phase-shifting interferometry using the concept of a data-sampling window. *Applied Optics , 34*, 4723-4730.

Groot, P. J. (1994). Extending the unambiguous range of two-color interferometers. *Applied Optics , 33*, 5948–5953.

Groot, P. (2000). Measurement of transparent plates with wavelength-tuned phase-shifting interferometry. *Applied Optics , 39*, 2658–2663.

Han, G. S., & Kim, S. W. (1994). Numerical correction of reference phase in phase shifting interferometry by iterative least-square fitting. *Applied Optics , 33*, 7321-7325.

Hariharan, P. (2003). *Optical interferometry* (2nd ed.). Academic Press.

Hariharan, P., Oreb, B. F., & Eiju, T. (1987). Digital phase-shifting interferometry: a simple error-compensation phase calculation algorithm. *Applied Optics , 26*, 2504-2506.

Hartmann, L., Hagen, K. M., & Zeid, A. A. (2008). An absolute distance interferometer with two external cavity diode lasers. *Measurement Science and Technology , 19*, 1-6.

Harvey, K. C., & Myatt, C. J. (1991). External-cavity diode laser using a grazing-incidence diffraction grating. *Optics Letters , 16*, 190-192.

Hibino, K., Tani, Y., Bitou, Y., Takatsuji, T., Warisawa, S., & Mitsuishi, M. (2010). Discontinuous surface measurement by wavelength-tuning interferometry with the excess fraction method correcting scanning nonlinearity. *Applied Optics , 50*, 962-969.

HighFinesse. (2011). *WS7 wavelength meter*. Retrieved from http://www.highfinesse.com/en/wavelengthmeter/ws7.php

http://www.coherix.com/automotive. (2011).

Huang, K. Y., & Carter, G. M. (1994). Coherent optical frequency domain reflectometry (OFDR) using a fiber grating external cavity laser. *IEEE Photonics Technology Letters , 6*, 1466-1468.

Iiyama, K., Wang, L. T., & Hayashi, K. (1996). Linearizing optical frequency-sweep of a laser diode for FMCW reflectometry. *Journal of Lightwave Technology , 14*, 173-178.

ISO. (1995). *Guide to the Expression of Uncertainty in Measurement International Organization for Standardization.* Geneva, Switzerland.

Jin, J., Kim, Y. J., Kim, U., & Kim, S. W. (2006). Absolute length calibration of gauge blocks using optical comb of a femtosecond pulse laser. *Optics Express , 14*, 5968-5974.

Joo, K. N., & Kim, S. W. (2006). Absolute distance measurement by dispersive interferometry using a femtosecond pulse laser. *Optics Express , 14*, 5954-5960.

Kafri, O., & Glatt, I. (1989). *The Physics of Moire Metrology.* John Wiley & Sons.

Kikuta, H., & Nagata, R. (1987). Absolute distance measurement by wavelength shift interferometry with a laser diode: some systematic error sources. *Applied Optics , 26*, 1654-1660.

Kikuta, H., Iwata, K., & Nagata, R. (1986). Distance measurement by the wavelength shift of laser diode light. *Applied Optics , 25*, 2976-2980.

Kilpelä, A., Pennala, R., & Kostamovaara, J. (2001). Precise pulsed time-of-flight laser range finder for industrial distance measurements. *Review of Scientific Instruments , 72*, 2197-2202.

Kinder, T., & Salewski, K. D. (2002). Absolute distance interferometer with grating stabilized tunable diode laser at 633 nm. *Journal of Optics A; Pure Applied Optics , 4*, 364-368.

Kinnstaetter, K., Lohmann, A. W., Schwider, J., & Streibl, N. (1988). Accuracy of phase shifting interferometry. *Applied Optics , 27*, 5082-5089.

Kobayashi, M., Takada, K., & Noda, J. (1990). Optical-frequency encoder using polarization-maintaining fiber. *Journal of Lightwave Technology , 8*, 1697-1702.

Krishnamachari, V., Andresen, E. R., Keiding, S. R., & Potma, E. O. (2006). An active interferometer-stabilization scheme with linear phase control. *Optics Express , 14*, 5210-5215.

Lassahn, G. D., Lassahn, J. K., Taylor, P. L., & Deason, V. A. (1994). Multiphase fringe analysis with unknown phase shifts. *Optical Engineering , 33*, 2039-2044.

Lewis, A. D. (1993). *Absolute length measurement using multiple-wavelength phase-stepping interferometry.* University of London.

Littman, M. G., & Metcalf, H. J. (1978). Spectrally narrow pulsed dye laser without beam expander. *Applied Optics , 17*, 2224-2227.

Liu, K., & Littman, M. G. (1981). Novel geometry for single-mode scanning of tunable lasers. *Optics Letters , 6*, 117-118.

Lu, S. H., & Lee, C. C. (2002). Measuring large step heights by variable synthetic wavelength interferometry. *Measurement Science and Technology , 13*, 1382-1387.

Lu, S. H., Chiueh, C., & Lee, C. C. (2002). Differential wavelength-scanning heterodyne interferometer for measuring large step height. *Applied Optics , 41*, 5866-5871.

Luecke, F. S. (1994). *Patent No. 5319668.* U. S.

Margheri, G., Giunti, C., Zatti, S., Manhart, S., & Maurer, R. (1997). Double-wavelength superheterodyne interferometer for absolute ranging with submillimeter resolution: results obtained with a demonstration model by use of rough and reflective targets. *Applied Optcis , 36*, 6211-6216.

Marron, J. C. (2000). Three-dimensional imaging using a tunable laser source. *Optical Engineering , 39*, 47-51.

Marron, J. C., & Schroeder, K. S. (1992). Three-dimensional lensless imaging using laser frequency diversity. *Applied Optics , 31*, 255-262.

Massig, J. H., & Heppner, J. (2001). Fringe-pattern analysis with high accuracy by use of the Fourier-transform method: theory and experimental tests. *Applied Optics , 40*, 2081-2088.

Matsumoto, H. (1981). Infrared He-Xe laser interferometry for measuring length. *Applied Optics , 20*, 231-234.

Minoshima, K., & Matsumoto, H. (2000). High-accuracy measurement of 240-m distance in an optical tunnel by use of a compact femtosecond laser. *Applied Optics , 39*, 5512-5517.

Moore, E. D., & McLeod, R. R. (2008). Correction of sampling errors due to laser tuning rate fluctuations in swept-wavelength interferometry. *Optics Express , 16*, 13139-13149.

Okada, K., Sakuta, H., Ose, T., & Tsujiuchi, J. (1990). Separate measurements of surface shapes and refractive index inhomogeneity of an optical element using tunable-source phase shifting interferometry. *Applied Optics , 29*, 3280–3285.

Olsson, A., & Tang, C. L. (1981). Dynamic interferometry techniques for optical path length measurements. *Applied Optics , 20*, 3503-3507.

Pförtner, A., & Schwider, J. (2003). Red-green-blue interferometer for the metrology of discontinuous structures. *Applied Optics , 42*, 667-673.

Phillion, D. W. (1997). General methods for generating phase-shifting interferometry algorithms. *Applied Optics , 36*, 8098-8115.

Polhemus, C. (1973). Two-Wavelength Interferometry. *Applied Optics , 12*, 2071-2074.

Pollinger, F., Hagen, K. M., Wedde, M., & Zeid, A. A. (2009). Diode-laser-based high-precision absolute distance interferometer of 20 m range. *Applied Optics , 48*, 6188-6194.

Saldner, H. O., & Huntley, J. M. (1997). Temporal phase unwrapping: application to surface profiling of discontinuous objects. *Applied Optics , 36*, 2770-2775.

Salvadé, Y., Schuhler, N., Lévêque, S., & Floch, S. L. (2008). High-accuracy absolute distance measurement using frequency comb referenced multiwavelength source. *Applied Optics , 47*, 2715-2720.

Sasaki, O., Yoshida, T., & Suzuki, T. (1991). Double sinusoidal phase modulating laser diode interferometer for distance measurement. *Applied Optics , 30*, 3617-3621.

Schmidt, J., & Creath, K. (1992). Spatial and temporal phase measurement techniques: a comparison of major error sources in one dimension. *Interferometry: Techniques and Analysis. 1755*, pp. 202-211. Proceedings of SPIE.

Schuhler, N., Salvadé, Y., Lévêque, S., Dändliker, R., & Holzwarth, R. (2006). Frequency-comb-referenced two-wavelength source for absolute distance measurement. *Optics Letters , 31*, 3101-3103.

Schwider, J. (1988). *Real-time methods in optical testing interferometry.* ZOS Report.

Schwider, J., Burrow, R. E., Grzanna, J., Spolaczyk, R., & Merkel, K. (1983). Digital wavefront measuring interferometry: some systematic error sources. *Applied Optics , 22*, 3421-3432.

Stone, J., & Stejskal, A. (1998). Absolute interferometry with a 670-nm external cavity diode laser. *Applied Optics , 44*, 3937-3944.

Su, X., & Chen, W. (2004). Reliability-guided phase unwrapping algorithm: a review. *Optics and Lasers in Engineering , 42*, 245-261.

Suematsu, M., & Takeda, M. (1991). Wavelength-shift interferometry for distance measurements using the Fourier transform technique for fringe analysis. *Applied Optics , 30*, 4046-4055.

Surrel, Y. (1993). Phase stepping: a new self-calibrating algorithm. *Applied Optics , 32*, 3598-3600.

Takeda, M., Ina, H., & Kobayashi, K. (1982). Fourier-transform method of fringe pattern analysis for computer-based topography and interferometry. *Optical Society of America , 72*, 156-160.

Tansey, R. J. (1983). An absolute distance interferometer using a dye laser heterodyne interferometer and spatial separation of beams. In J. C. Wyant (Ed.), *Precision Surface Metrology. 429*, pp. 43-54. Proceedings of SPIE.

The velocity tunable diode laser: Model 6300 user's manual. (2000).

Thiel, J., Pfeifer, T., & Haas, C. (1995). Interferometric measurement of absolute distance up to 40 m. *Measurement , 16*, 1-6.

Tiziani, H. J., Rothe, A., & Maier, N. (1996). Dual-wavelength heterodyne differential interferometer for high-precision measurements of reflective aspherical surfaces and step heights. *Applied Optics , 35*, 3525-3533.

Towers, C. E., Towers, D. P., & Jones, J. C. (2003). Optimum frequency selection in multifrequency interferometry. *Optics Letters , 28*, 887-889.

Trolinger, J. D. (1996). Ultrahigh Resolution Interferometry. *Proceedings of the SPIE , 2861*, pp. 114-123.

Tsuji, K., Shimizu, K., Horiguchi, T., & Koyamada, Y. (1997). Spatial-resolution improvement in long-range coherent optical frequency domain reflectometry by frequency-sweep linearisation. *Electronics Letters , 33*, 408-410.

Vakhtin, A. B., Kane, D. J., Wood, W. R., & Peterson, K. A. (2003). Common-Path Interferometer for Frequency-Domain Optical Coherence Tomography. *Applied Optics , 42*, 6953-6958.

Vander, R., Lipson, S. G., & Leizerson, l. (2003). Fourier fringe analysis with improved spatial resolution. *Applied Optics , 42*, 6830-6837.

Vaughan, J. M. (1989). *The Fabry-Perot interferometer : history, theory, practice and applications.*

Waagaard, O. H. (2005). Spatial characterization of strong fiber Bragg gratings using thermal chirp and opticalfrequency-domain reflectometry. *Journal of Lightwave Technology , 23*, 909-914.

Walsh, C. J. (1987). Limit to multiwavelength interferometry imposed by frequency instability of the source. *Applied Optics , 26*, 29-31.

Wan, G., & Nosekabel, E. H. (1999). Surface Inspection on Bodies in White in AutomotiveIndustry. *Proceedings of SPIE, 3824*, pp. 329-333.

Wang, L. T., Iiyama, K., Tsukada, F., Yoshida, N., & Hayashi, K. I. (1993). Loss measurement in optical waveguide devices by coherent frequency-modulated continuous-wave reflectometry. *Optics Letters , 18*, 1095-1097.

Wykes, C., & Morshedizadeh, R. (1995). Surface Topography Measurement Using Digital Moiré Contouring – Errors and Limitations. *Proceedings of the Institution of Mechanical Engineers, Part B: Journal of Engineering Manufacture , 209*, 317-325.

Xiaoli, D., & Katuo, S. (1998). High-accuracy absolute distance measurement by means of wavelength scanning heterodyne interferometry. *Measurement Science and Technology , 9*, 1031-1035.

Yang, H. J., Deibel, J., Nyberg, S., & Riles, K. (2005). High-precision absolute distance and vibration measurement with frequency scanned interferometry. *Applied Optics , 44*, 3937-3944.

Ye, J. (2004). Absolute measurement of a long, arbitrary distance to less than an optical fringe. *Optics Letters , 29*, 1153-1155.

Yu, H., Aleksoff, C. C., & Ni, J. (To be submitted). Thickness measurement of transparent plates by wavelength stepping interferometry and a multiple height-transfer interferometric technique. *Applied Optics* .

Yu, H., Aleksoff, C., & Ni, J. (2011). A multiple height-transfer interferometric technique. *Optics Express , 19*, 16365-16374.

Yu, H., Aleksoff, C., & Ni, J. (to be submitted). Accuracy of a multiple height-transfer interferometric technique for absolute distance metrology. *Applied Optics* .

Zhu, S. (1989). Developed method of excess fractions for calibrating the effective optical thickness of a Fabry-Perot etalon. *Journal of the Optical Society of America , 6*, 500-507.

Zollne, F., Matusevich, V., & Kowarschik, R. (2003). 3D Measurement by Stereophotogrammetry. *Proceedings of the SPIE on Optical Measurement Systems for Industrial Inspection III*, *5144*, pp. 311-314.

Zou, D., Ye, S., & and Wang, C. (1995). Structured-Lighting Surface Sensor and Its Calibration. *Optical Engineering , 34*, 3040-3043.